Journal of Materials Science & Technology 203 (2024) 180–200

Contents lists available at ScienceDirect

Journal of Materials Science & Technology

journal homepage: www.elsevier.com/locate/jmst

Research Article

# Recent advances in synchrotron X-ray studies of the atomic structures of metal alloys in liquid state

Shi Huang[a,b], Kang Xiang[a], Jiawei Mi[a,c,*]

[a] School of Engineering, University of Hull, Hull, HU6 7RX, UK
[b] School of Engineering and Westlake Institute for Advanced Study, Westlake University, Hangzhou 310030, China
[c] School of Materials Science and Engineering, Shanghai Jiao Tong University, Shanghai 200240, China

ARTICLE INFO

*Article history:*
Received 14 November 2023
Revised 17 January 2024
Accepted 7 February 2024
Available online 13 April 2024

*Keywords:*
Synchrotron X-rays
Atomic structures
Metal alloys
Liquid state
Molecular Dynamics modelling

ABSTRACT

Research into the atomic structures of metal materials in the liquid state, their dynamic evolution versus temperature until the onset of crystal nucleation has been a central research topic in condensed matter physics and materials science for well over a century. However, research and basic understanding of the atomic structures of liquid metals are far less than those in the solid state of the same compositions. This review serves as a condensed collection of the most important research literature published so far in this field, providing a critical and focused review of the historical research development and progress in this field since the 1920s. In particular, the development of powerful synchrotron X-ray sources and the associated experimental techniques and sample environments for studying in-situ the atomic structures of different metallic systems. The key findings made in numerous pure metals and metallic alloy systems are critically reviewed and discussed with the focus on the results and new understandings of structural heterogeneities found inside a bulk liquid, at the liquid surface or liquid-solid interface. The possible future directions of research and development on the most advanced experimental and modeling techniques are envisaged and briefly discussed as well.



## 1. Introduction

Liquid is one of the four fundamental states of matter (i.e., gas, liquid, solid, and plasma) that occurs naturally in the universe [1]. Liquid materials or materials in their liquid state are ubiquitous in nature [2,3]. The properties and functionalities of a liquid material are predominantly determined by its constituent atoms, the bonding and interactions among these atoms, and the atomic structures formed by adapting to its surrounding environment and the thermodynamic driving forces, for example, gravitational force, temperature, pressure [4], electromagnetic fields [5], ultrasonic fields [6], etc. [2]. For the metal-based materials, which are the main focus of this review paper, most of them are in the solid state at room temperature and atmospheric pressure in the earth's surface environment [7]. Only one pure metal has its melting temperature below room temperature (Hg @ −38.83 °C) and another one slightly above room temperature (Ga @ 29.76 °C) [7]. In general, heating up a metal material above its melting point and then mixing it with other constituent materials is the most effective way of producing new metal material systems or alloys [8]. The heating processes may occur naturally due to firing or volcano eruption, or through a controlled heating method or system purposely developed by human beings [9]. The uses of firing for the smelting of metals have been a crucial step in the development of man-made metal materials in human civilization history and even today. Metal materials in their liquid state are crucial because their atomic structures are the basis for any subsequent structure development in the solid state [10–12]. Unfortunately, research and basic understanding of the atomic structures of liquid metals are far less than those in the solid state of the same compositions. This review serves as a condensed collection of the most important research literature published so far in this field, providing a critical and focused review on the historical research development and progress in this field since the 1950s. The outlook and possible future research directions are also discussed and envisaged.

* Corresponding author.
*E-mail address:* j.mi@hull.ac.uk (J. Mi).

https://doi.org/10.1016/j.jmst.2024.02.038

## 2. A brief overview of the research on liquid metals

### 2.1. Special melting techniques for studying liquid metal structures

Solid metals need to be melted above their melting points to be in the full liquid state [9]. The most common techniques for melting solid metals are to place the metallic charges inside a container (crucible) and then heat up the crucible by using gas/oil fire, hot bath/air, or electricity via resistance or induction heating mechanism [9]. However, in those methods, a part of the molten metals is in direct contact with the crucible wall, which may affect or limit what type of probes can be used for collecting the data that contain the liquid metal structure information [13]. Hence a number of levitation methods were developed in the past to first melt the metals without the use of a conventional crucible (e.g., just using a holding plate) and then to lift and hold the molten liquids in a free space via a counter-gravity force [14–17]. The most common and effective methods are (1) aerodynamic levitation [18–23], (2) electromagnetic levitation [18,24–27], (3) electrostatic levitation [13,28–33], and (4) acoustic levitation [34,35] as described briefly in this section. In addition, for minimizing the effects of gravity, melting and solidification experiments have been also carried out in a microgravity environment onboard sounding rockets at a distance of ~100 km above the Earth's surface [36,37].

#### 2.1.1. Aerodynamic levitation

In 1969, Beard et al. [22] made the first attempt to explore the aerodynamic levitation (ANL) method to levitate and then study $\mu$m-to-mm diameter water drops in a wind tunnel. ANL uses the floating force of a gas streaming flow through a convergent-divergent nozzle to levitate a sample against gravity. Fig. 1(a, b) shows a typical example of such an aerodynamic levitator. Laser beams are often used to heat the sample, avoiding any direct contact between the sample and the container's wall during melting [23]. This method has been widely used in studying metal oxides, but, to a lesser extent, in studying metal alloys and semiconductors [38]. The advantage of ANL is that it is applicable to any liquid materials on the condition that the right gas medium was chosen according to the type of metals to be melted. However, there is always a layer of high-speed gas flowing around the liquid, which may interfere with the probe or sensor for acquiring the structure data information from the liquid.

#### 2.1.2. Electromagnetic levitation

For electrically conductive metal samples, levitation of the liquid material against gravity can be achieved by imposing an electromagnetic field around the sample, e.g., using a high-frequency alternating inhomogeneous electromagnetic field generated by a water-cooled Cu coil [15]. In 1923, Muck [39] did one of the earliest electromagnetic levitation (EML) melting experiments.

Then Okress et al. [41] made further improvements on EML in the 1950s. In 1998, Jacobs et al. [26,27] applied the EML technique for the first time at beamline BM29 of the European Synchrotron Radiation Facility (ESRF). They investigated successfully the short-range order (SRO) structures of the Co80Pb20 alloy in the liquid state. Fig. 1(c, d) shows the schematic of the electromagnetic levitator integrated at BM29. In addition to the uses of X-ray, neutron is another very commonly used radiation beam to study the atomic structures of electromagnetically levitated alloy melts [42–44].

#### 2.1.3. Electrostatic levitation

For a charged or polarized sample, levitation can be achieved by exploiting the Coulomb force [15]. For example, two capacitor plates can be arranged in parallel with a certain distance apart, generating a vertical electric field between the two plates, which can levitate a charged sample against gravity and this is normally

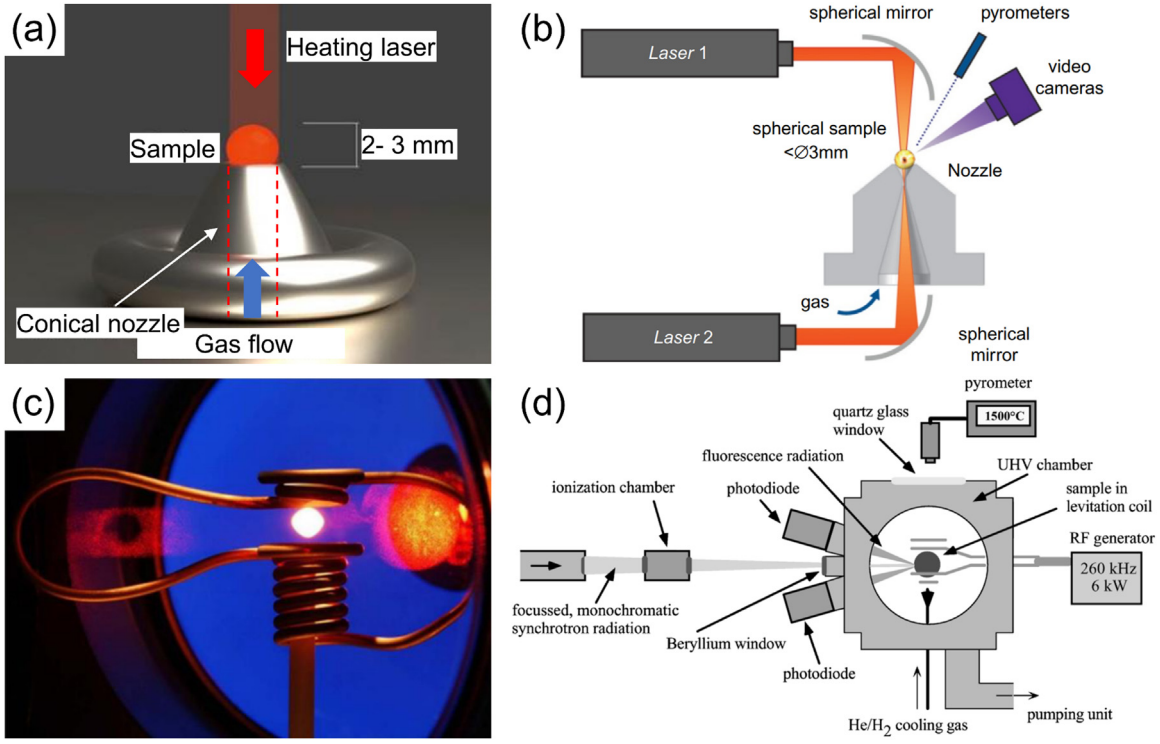


**Fig. 1.** (a) An image [40] and (b) a schematic, showing a typical aerodynamic levitator and the $CO_2$ lasers for heating samples [38]. A spherical liquid sample is floating on top of a gas stream passing through a nozzle. (c) A liquid metal droplet levitated electromagnetically by the field generated by the Cu coil [38] and (d) a sectional view of the EML furnace used at BM29 of the ESRF [26].

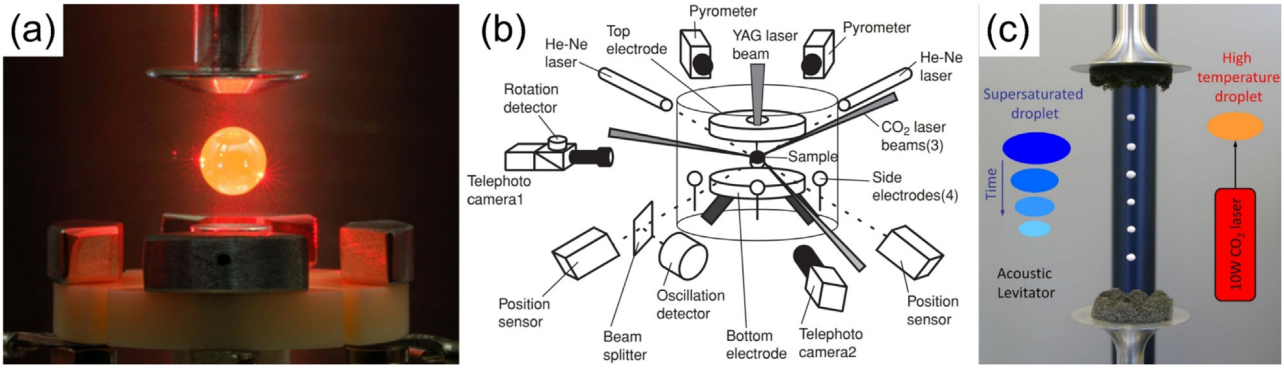


**Fig. 2.** (a) An image of an electrostatically levitated $Ti_{39.5}Zr_{39.5}Ni_{21}$ droplet at 1150 K. The spherical sample is floating between two vertical electrodes [31]. (b) A Schematic of the ESL furnace [13]. A pair of parallel disc electrodes are placed inside a stainless-steel chamber with ~$10^{-5}$ Pa pressure, between which a charged sample is levitated. (c) A typical scenario of an acoustic levitator used at 11-ID-C of APS. The illustrations on both sides of the levitator show the methods of forming amorphous pharmaceutical drugs [34].

called electrostatic levitation (ESL) [15]. However, it has an inherent instability issue that needs to have a fast feedback loop control in place so as to correct any deviation away from the preset position [33].

In 1988, the European Space Agency (ESA) performed the first microgravity experiment in a sounding rocket (TEXUS-19), attempting to electrostatically levitate and melt a glass-forming material (24 mol% $Li_2O$–76 mol% $SiO_2$) [45]. However, this attempt was unsuccessful because of the difficulty in controlling the sample position.

In 1993, Rhim invented the first ESL apparatus at NASA's Jet Propulsion Laboratory [33]. The ESL was further improved at Caltech to reduce the temperature gradient across a liquid sample and to increase the stability of sample positioning with a tetrahedral laser heating system [46]. Fig. 2(a, b) shows the typical scenarios of electrostatically levitated metal droplets. Since then, it has become the preferred method to study the thermo-physical properties of liquid metal alloys and to investigate the crystal nucleation dynamics in different liquids [13,28–32,47].

#### 2.1.4. Acoustic levitation

Acoustic levitation is realized by utilizing the acoustic radiation pressure from high-intensity ultrasound. In 1933, Bucks et al. [48] made the first attempt at acoustic levitation. The next progress came in 1949 when Hilary tried to apply acoustic radiation to the agglomeration of dust particles in mining [49]. Then, in 1985, Trinh et al. [50] further developed the concept and the associated device for studying fluid dynamics. Fig. 2(c) shows a typical acoustic levitator used by Benmore et al. [23] at beamline 11-ID-C of the Advanced Photon Source (APS). However, due to the limited lifting force and the need for the gas medium for ultrasound transmission and appropriate heating sources, acoustic levitation has been hardly used for the studies of liquid metals.

In summary, ANL and acoustic levitation can easily levitate non-conducting materials, while EML is only suitable for levitating conductive metal materials, but these three methods often cause distorted shape on the sample surface (i.e., deviated from a spherical shape), which could be a problem in accurately measuring the surface properties of the liquids. ANL also needs high-speed gases to levitate a molten sample against gravity and cool the sample. However, the impurities in the gases might contaminate the samples, which not only reduces the degree of undercooling but also affects the surface properties [51]. In contrast, due to the rapid upgrading of the ESL hardware and software setup [51], the well-developed ESL has been widely used to study the structure of liquid metals at synchrotron and neutron beamlines around the world [28–32,52].

### 2.2. Scientific focuses of the research on liquid metal structures

Depending on the types of atomic species, pressure, and temperature conditions as well as the local surrounding environment, liquid metals may have distinctly different atomic structures as briefly described in this section.

#### 2.2.1. Atomic structure of liquid metal surface

When a liquid metal is in direct contact with different gases, e.g., with air, inert gases, or even a vacuum environment, the atomic structure of the surface of the liquid metal is different from that of the bulk liquid. In 1999, Tostmann et al. [53] and Dimasi et al. [54] investigated the surface structures of liquid Hg, Ga, and In using the X-ray reflectivity technique. They found that the liquid surface has a different structural order compared to that of the bulk liquid, and the interatomic interactions in liquid metals are strongly dependent on the electronic structure.

In 2005, Oh et al. [55] observed the infiltration of oxygen from the microscope column into the well-organized liquid along the interface using high-resolution transmission electron microscopy (TEM). $Al_2O_3$ was formed through epitaxial growth, driven by the dynamic motion of interfacial steps. This is crystal-induced orderings of liquids that occurred during the process of liquid phase epitaxial growth and high-temperature wetting. Furthermore, Gandman et al. [56] also used aberration-corrected TEM to investigate in situ the interfaces between liquid Al and various sapphire facet planes and confirmed the more ordered nature of the liquid at the interface which is dependent on the sapphire facet planes. For example, the degree of ordering decreased on the planes of $\{0006\} > \{1\bar{2}10\} > \{10\bar{1}2\} \geq \{\bar{1}014\}$. Further studies in AlCu [57] and AlNi [58] systems also confirmed that there is indeed a correlation between the structure of the solid surface and the ordering of the adjacent liquid, which is essential for a more quantitative understanding of solid-liquid interfaces.

#### 2.2.2. Atomic structure of bulk liquid metal and liquid-to-liquid structure transition

Moving away from the surface and into the bulk volume of a liquid metal of the same and homogenous composition, for any reference atom in a completely disordered system, the local surrounding atomic environment could be assumed as the same from statistical point of view. However, such local atomic environment is strongly linked to the local temperature of the liquid as well as the local composition. If the temperature or composition is not homogenous, there may exist different atomic configurations or distributions of different species in different regions of the bulk volume which may develop into metastable and/or polymor-

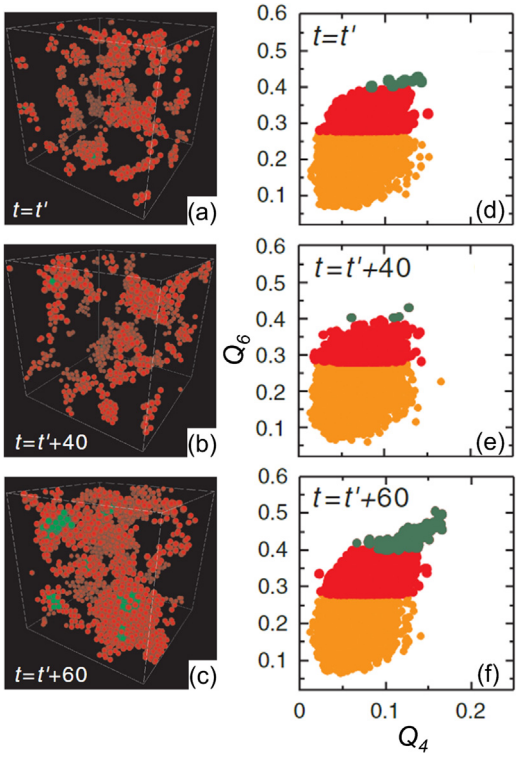


**Fig. 3.** (a–c) Snapshot of the FCC crystal nucleus transferred from MROs at $t = t'$, $t = t' + 40$, and $t = t' + 60$. (d–f) The corresponding temporal bond-orientational order analysis. Time $t = t'$ is when a supercooled liquid reaches a sort of quasi-equilibrium steady state after the initiation of simulations from a random disordered state [74].

phous structures. Such inhomogeneous and metastable structures are very common in superheated liquid metals when cooled with different cooling rates. Understanding the geometrical characteristics of such metastable atomic structures and their evolution versus temperature has been a long-time and very important research topic in condensed matter physics and materials science disciplines for well over a century.

In this aspect, Brodova et al. [11] demonstrated that above the liquidus and dependent on the level of superheating, there is a gradual structure transformation in the liquid metals. Such structure inhomogeneity (or heterogeneity) is reflected in the SRO and/or MRO atomic clusters which in turn greatly affect the subsequent crystal nucleation and solidified structures [59–61]. This serves as the new theoretical framework for understanding crystallization. Recent experimental [62–66] and simulation studies [67–71] have revealed progressively that, in the liquid state, the atomic structures are not isotropic and homogeneous. It may have more complex and heterogeneous structures with local spatial regions of different geometrical characteristics and mobility [62,72,73]. For example, in 2010, Kawasaki and Tanaka [74] revealed that a supercooled colloidal liquid is actually not homogeneous, but has transient medium-range structural order. They found nucleation preferentially took place in regions of high structural order via wetting effects, which reduce the crystal–liquid interfacial energy significantly and thus promote crystal nucleation. Fig. 3 illustrates how FCC crystal nucleated in a supercooled state of the hard-sphere (colloidal) system. The bond orientational order before crystal nucleation ($t = t'$) is characterized by HCP-like symmetry (red atoms in Fig. 3(a–c); the red dot on the $Q_4 - Q_6$ map), whereas the crystals nucleated have a mixed character of HCP and FCC-like order (the green atoms in the simulation box and green dots on the map). When $t = t' + 60$ ns, the pre-ordered atoms (red) connect with each other, forming MROs. The crystallinity degree ($Q_4$) of the system increased as well as the lattice match degree ($Q_6$), forming the primary nuclei. Hence, nucleation is a multi-step process prior to the formation of a new crystal.

The conventional view of an isotropic single atomic structure in the liquid state is an over-simplistic model, even a single element liquid may exhibit more than two distinct liquid states. The transitions between these different liquid states are characterized as 'liquid-liquid transitions' (LLT) [3], which may be characterized by the evolutions of the SRO and/or MRO atomic clusters versus temperature (or pressure). The transition within the liquid state may lead to changes or variations in some of the physical properties, e.g., viscosity [75,76], internal friction [77], magnetic susceptibility [78,79], etc. Therefore, it is paramount to understand the mechanisms and to elucidate the influence of LLT on the nucleation process.

Some studies indicate that LLT in the liquid state might induce unexpected modifications in the degree of undercooling [79,80]. They demonstrated that at a higher superheat temperature, thermal-induced diffusion intensifies, leading to more uniformly distributed alloying elements [40]. The homogenization of melt is often accompanied by the dissolution of atomic clusters, leading to a higher effective undercooling. An increase in undercooling leads to the formation of a supersaturated solid solution of the alloying elements. During the cooling of a superheated melt, the LLT may occur, producing more ordering in the liquid phase.

Nevertheless, no direct experimental observation of the clusters' behavior in superheated bulk liquid metals has been reported. Real-time synchrotron X-ray and neutron diffraction experiments are crucial for providing the experimental evidence, in particular, the statistic information for the local liquid structure, e.g., pair distribution function, mean bond length and coordination number, etc. The development of precise models for liquid structures, particularly in systems exhibiting LLT, is paramount for advancing the basic understanding.

### *2.2.3. Atomic structure evolution versus temperature and onset of crystal nucleation*

For most metallic materials, especially the man-made technical alloys that have been designed and developed so far, the primary goal of studying their atomic structures in the liquid states is to provide a scientific understanding of how such structures influence the atomic structures during the liquid-to-solid phase transformation processes and ultimately the structures in the solid state which determine the final properties and/or functionalities of the materials [11].

When a liquid metal is cooled down below its melting temperature, its structure may undergo two possible transformations: vitrification or crystallization [81] (see Fig. 4). Vitrification is when the liquid structure is "frozen" into the solid state and maintains the random atom arrangement from the liquid state. In 1836, Louis Gay-Lussac first observed the vitrification phenomenon [82]. He discovered the phenomenon of supercooling when water was found to maintain its liquid structure at a temperature below the freezing point. Almost a century later, in 1938, Luyet [83,84] published the first report and defined the term "vitrification".

Crystallization is a multi-step phase transition process with several stages: transitioning from a disordered amorphous structure to a pre-ordered structure, and the development of stable crystal nuclei that grow into an ordered (or distorted) lattice structure. This entire process is governed by the thermodynamic driving forces within the system. It is a dynamic process to move towards a lower and stable energy state.

The well-established Classical Nucleation Theory (CNT) describes the formation of nuclei from the dynamic and stochastic association of monomeric units (e.g., ions, atoms, or molecules)

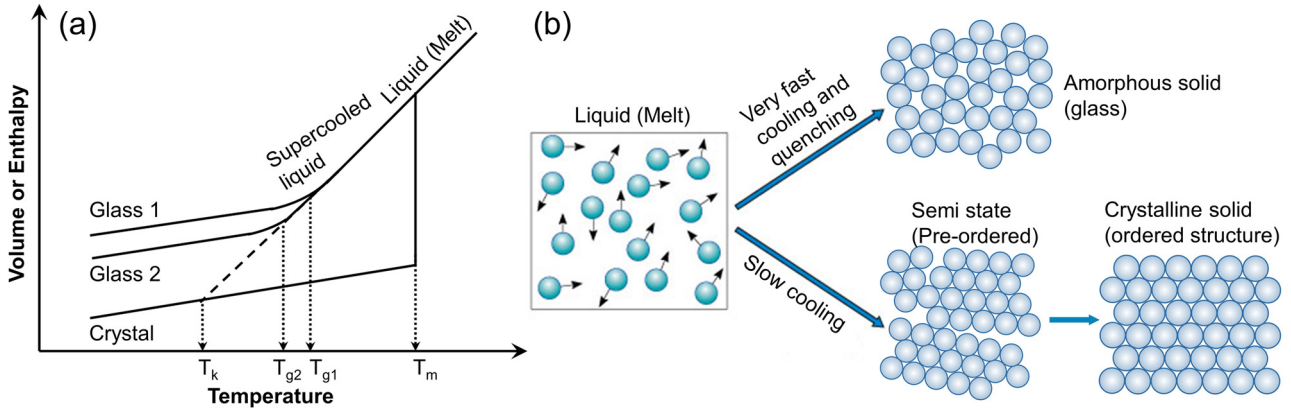


**Fig. 4.** (a) The relationship of enthalpy (or volume) versus temperature of a liquid melt during the crystallization or vitrification (glassy transition) process at different cooling rates ($T_k$: Kauzmann temperature, $T_g$: glass transition temperature, $T_m$: fusion temperature) [85]. (b) The transition pathway of "vitrification" and "crystallization".

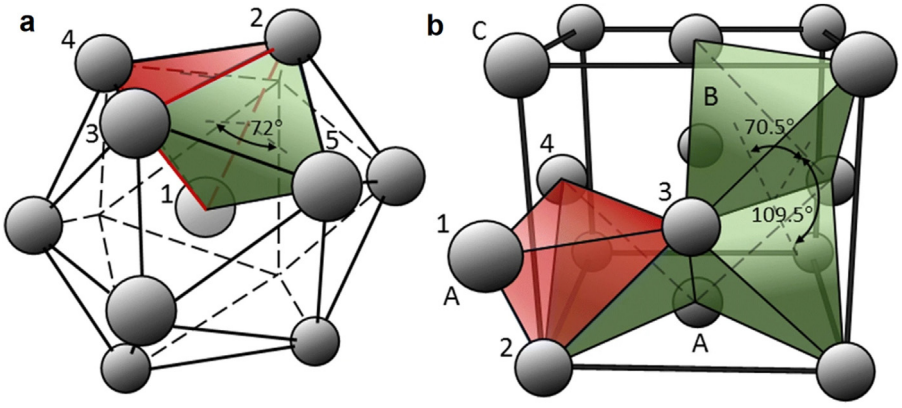


**Fig. 5.** (a) An icosahedron with two nearest-neighbors of its 20 tetrahedra shown in red and green; (b) a unit cell of the FCC structure with the representation of 3 of the 8 tetrahedra made of (1 1 1) planes and 〈110〉 edges (in green) and one stacking fault induced by the attachment of one tetrahedron (in red) [96].

that overcome a free-energy barrier at a critical nucleus size and grow out to a mature bulk phase in a homogeneous liquid [86–88]. In the crystallization pathway, to overcome the energy barrier for initiating crystal nuclei, the liquid needs to be undercooled below its equilibrium melting temperature. However, more and more experiments [62–65] and computational studies [67–70] have indicated that liquid structure is not homogeneous, it may have more complex and heterogeneous structures with local spatial regions of different geometrical characteristics and mobility [11,62,72,73]. Hence, understanding the dynamics of the disordered-to-ordered atomic structure transition in liquid metal systems at different thermodynamic conditions has been one of the central topics in condensed matter physics and materials science [74,89,90]. The competition between crystallization and vitrification is driven by many factors, including cooling rate, alloy compositions, and inherent stability of the liquid [91].

### 2.2.4. Atomic structure at the liquid-solid solidification front

After a solid crystal appears in the liquid, a liquid-solid interface forms with its local structural orderings between those of the crystal and liquid, adding interfacial energy that arises from configurations entropy difference between the liquid and crystal [92]. This often leads to a higher nucleation barrier and therefore higher degree of undercooling needed for nucleation to occur [92]. In 1950, Turnbull [93] demonstrated that metallic liquids could be cooled far below their equilibrium melting temperature without crystallization, suggesting a large energy barrier does exist in the formation of an ordered phase. This observation challenged Fahrenheit's assumption [94] that the barrier separating liquid and crystal phases in metals and alloys was small. In 1952, Frank [95] proposed that the undercooled metallic liquids have distinct local atomic structures with a significant degree of icosahedral short-range order (ISRO) (see Fig. 5(a)), which is incompatible with the extended periodicity of crystals (see the unit cell example in Fig. 5(b)). Compared to crystal structures, such as the Face Centred Cubic (FCC) and Body Centred Cubic (BCC) structures, the icosahedron has better rotational symmetry and more bonds. Therefore, in a cluster of 13 atoms, the icosahedron is a more energy-favorable geometrical arrangement than crystal structures, and it could be the dominant structure in monatomic liquids [96]. Such local structural difference between liquid and solid would result in a big configuration entropy difference and creates a barrier to crystal formation, explaining the observed undercooling behaviour.

### 2.2.5. Atomic structure of liquid at a heterogenous solid surface

In 2000, Reichert et al. [97] studied the structure of liquid Pb on a solid Si (0 0 1) surface (i.e., at the Si-Pb interface) by synchrotron X-ray diffraction at 600.6 K (10 K above its melting point). Fig. 6 shows a five-fold local symmetry of the liquid Pb at the Si (0 0 1) surface, providing the first direct experimental evidence for the existence of ISRO in liquid metals. Since then, ISRO was reported in undercooled Ni, Fe, and Zr liquids [24]. The above results confirmed Frank's hypothesis that ISRO does exist in undercooled liquids.

In 2003, Kelton et al. [28] observed the development of the ISRO in liquid $Ti_{39.5}Zr_{39.5}Ni_{21}$ during cooling, which reduced the nucleation barrier for the primary quasicrystal phase with five-

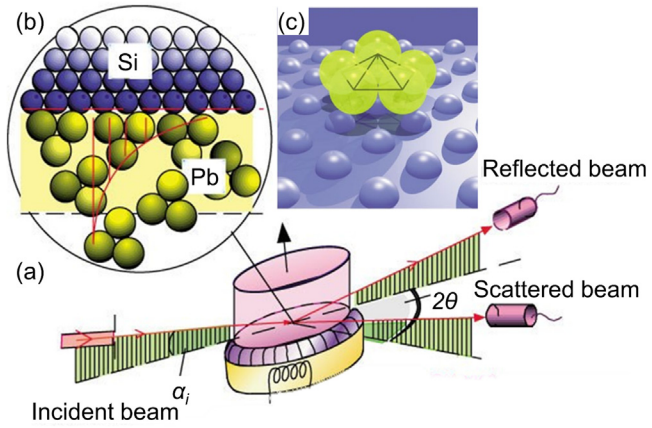


**Fig. 6.** (a) A synchrotron X-ray beam ($E$ = 71.5 keV, 8 μm spot size) penetrates the cylindrical Si solid ($r$ = 20 mm) from one side and impinges at grazing angles on the Pb–Si interface. For incidence angles below the critical angle of total internal reflection ($\alpha_c$ = 0.041°), the incident beam is totally reflected. (b) Enlarged area in the cylindrical interface, showing a specially designed ultrahigh vacuum (UHV) in situ diffraction chamber, the liquid Pb and the Si (001) surface are cleaned in UHV and then brought into contact at a temperature 10 K above the melting point of Pb. (c) Upper (pentagonal) half of the Pb icosahedron captured by the potential landscape of the primitive Si (001) surface [97].

fold symmetry. Such phase was metastable and would transfer to a stable crystal phase with further cooling. This was the first experimental evidence to link metastable ISRO to the crystal nucleation of a solid phase. After that, simulations on pure metals (Al [98], Fe [99], Ni [71,100,101], and Zr [102]) and binary alloy systems ($Cu_{50}Zr_{50}$ [102] and $Ni_{50}Al_{50}$ [102,103]) have also confirmed the presence of pre-ordered liquid atom clusters in the liquid state, which act as the precursors of crystal nuclei, facilitating nucleation or polymorphous development in the crystallization processes.

## 3. Experimental techniques for studying liquid metal structures

### 3.1. A brief overview of the development of synchrotron X-rays

Because of the opaqueness of liquid metals, high-energy X-rays, especially the high brilliance synchrotron X-rays, are the most commonly used techniques for studying atomic structures of liquid metals [3]. In 1968, the first dedicated synchrotron light source commenced operations at the Synchrotron Radiation Center, Tantalus, USA [104], marking the start of the era of synchrotron X-rays in all scientific disciplines.

The 1st generation synchrotrons had been built primarily for conducting high-energy particle physics experiments, while synchrotron light experiments were performed parasitically. In 1980, the first of the 2nd generation synchrotrons was built in the Daresbury Laboratory in the UK [106]. The 2nd generation of synchrotrons was solely dedicated to the production of synchrotron X-rays by using bending magnets and the X-rays have been used in almost all scientific disciplines ever since. In 1994, the European Synchrotron Radiation Facility (ESRF) in Grenoble, France became the first operational 3rd generation X-ray source in the world by exploiting the advantages of the special magnet arrays to optimize the intensity of the light produced. Together with the Advanced Photon Source (APS) at Argonne National Laboratory in the USA and the Spring-8 near Kyoto in Japan, these 3rd generation synchrotrons have revolutionized X-ray science in fields from nuclear physics to cultural heritage. Currently, there are more than 50 synchrotron light sources in the world (operational, or under construction) [107], including Shanghai Synchrotron Radiation Facility (SSRF) in China, Diamond Light Source (DLS) in the UK, SOLEIL in France, ALBA in Spain and NSLS-II in the US. In 2019, the ESRF started to upgrade to become the 4th generation synchrotron source characterized by an ultra-low emittance that approaches the diffraction limit, and thus called Extremely Bright Source (EBS) [108]. The 4th generation synchrotrons are capable of producing much more intense and tunable X-ray beams with brilliance and coherence one again by a factor of 100 [109]. The X-rays at these modern synchrotrons bridge the gap between visible light and electron microscopy, i.e., they give full access to study changes within heterogeneous atomic assemblies from ~$10^{12}$ atoms down to only a few atoms; all of this with spatial and temporal resolutions that approach a few atoms in space (nanometre to angstrom scale) and inter-atomic motion in time (nanosecond to femtosecond scale) respectively. Such incredible resolution and range in space and time are made possible by the absolutely impressive and never-ending improvements in the brightness, spectral range, and degree of spatial and temporal coherence and resolution of accelerator-based X-ray sources. During the last ~50 years peak-brightness has increased up to 22

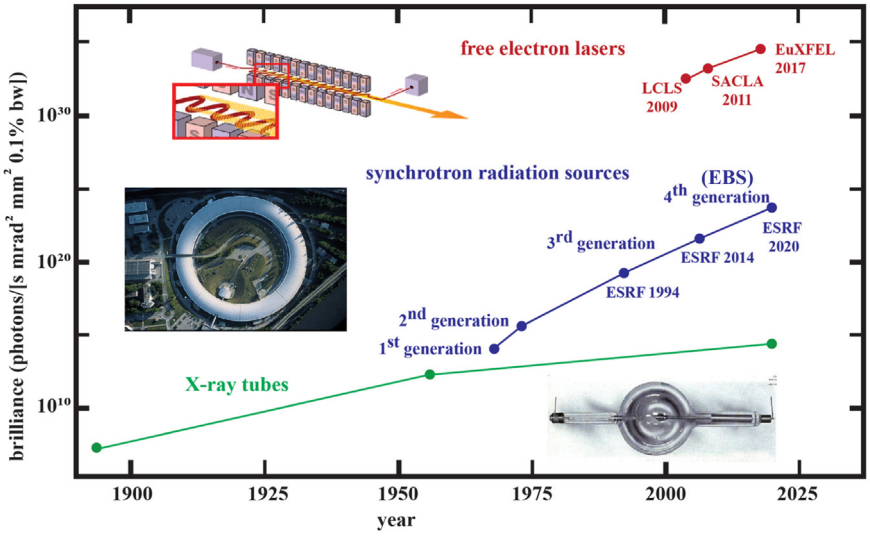


**Fig. 7.** Historical development of X-ray sources and their X-ray brilliance over time [105].

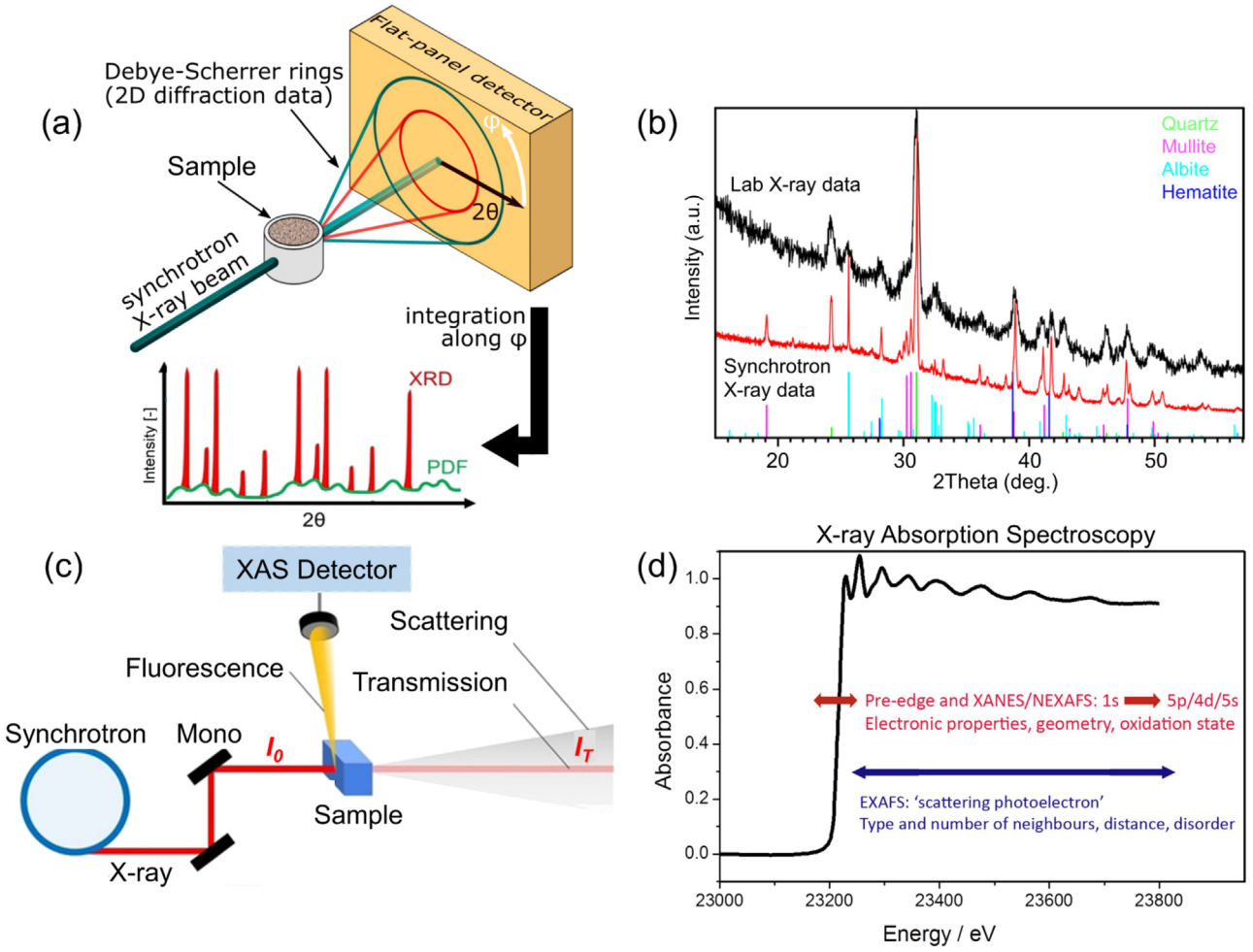


**Fig. 8.** (a) A schematic set-up of the in-situ synchrotron XRD experiment [112]. By azimuthal integration (along $\varphi$) of the Debye-Scherrer rings (2D diffraction data), 1D diffractograms were obtained. (b) Comparison of XRD patterns of brick fragments from a laboratory X-ray source ($\lambda$ = 1.79 Å, c. 3 h data collection, intensity multiplied by 15) and synchrotron X-ray source ($\lambda$ = 0.9534 Å, c. 1 h data collection) [113]. The quality of the XRD data produced from the synchrotron source was far superior to the laboratory source, both in terms of resolution and intensity. (c) A schematic set-up of in-situ synchrotron XAS measurement [114]. (d) Typical XAS spectrum with XANES and EXAFS regions identified.

orders of magnitude when compared to conventional laboratory sources [110].

When an X-ray beam is illuminating a material, its interactions with the material can generate useful information that is specific to this particular type of material. By collecting the information generated via different mechanisms, e.g., by scattering, transmission, or absorption using appropriate detectors, and then analyzing those data according to the well-established governing laws and/or databases, the structural and chemical information of the material can be determined. Here, we describe briefly the methods and associated instruments relevant to the research of liquid metals.

### 3.1.1. Synchrotron X-ray diffraction

Similar to the conventional laboratory X-ray diffraction (XRD), synchrotron XRD works on the same principle of Bragg's law. Fig. 8(a) shows that, in the diffracted 1D spectrum or 2D patterns, the constructive interferences (the sharp diffraction peaks – Bragg peaks) diffracted by crystal planes of the measured sample crystal lattice contain the averaged information about the long-range atomic structures in the scattering volume [111]. Fig. 8(b) shows that, due to the extremely high flux, tunable and well-defined wavelength, and better collimation of synchrotron radiation, Synchrotron XRD has much better sensitivity and higher resolution for the diffraction peaks than conventional laboratory XRD.

### 3.1.2. Synchrotron X-ray total scattering

Synchrotron X-ray total scattering (SXTS) spectrum contains the complete scattering pattern, including both Bragg and diffuse information [111]. In addition to the Bragg information, diffuse scattering in the patterns mainly arises from an irregular arrangement of atoms on the lattice sites that may contain some short-range ordering of the site occupancies or from the disordered arrangement of vacancies, interstitials, or impurity atoms [115,116]. Therefore, data reduction, background subtraction, and noise signal corrections are crucial for extracting the correct structural information from the scattering data, ensuring accurate and consistent analyses among different samples and experimental conditions. By far, the big limitation of high energy X-ray diffraction (scattering) is the rapidly decaying X-ray form factor signal compared to the background contribution (i.e., Compton scattering) at high-$Q$ values, making the accurate extraction of $S_X(Q)$ over the widest accessible $Q$-range problematic. At the highest $Q$-values, e.g., $> 30$ Å$^{-1}$, small corrections of less than one percent from the source, sample, and detector become magnified, leading to higher statistical and systematic errors, such that accurate normalization in absolute units becomes increasingly difficult [117].

### 3.1.3. Synchrotron X-ray absorption spectroscopy

Compared to the usual diffraction (scattering) methods, X-ray absorption spectroscopy (XAS), an absorption method, has the ad-

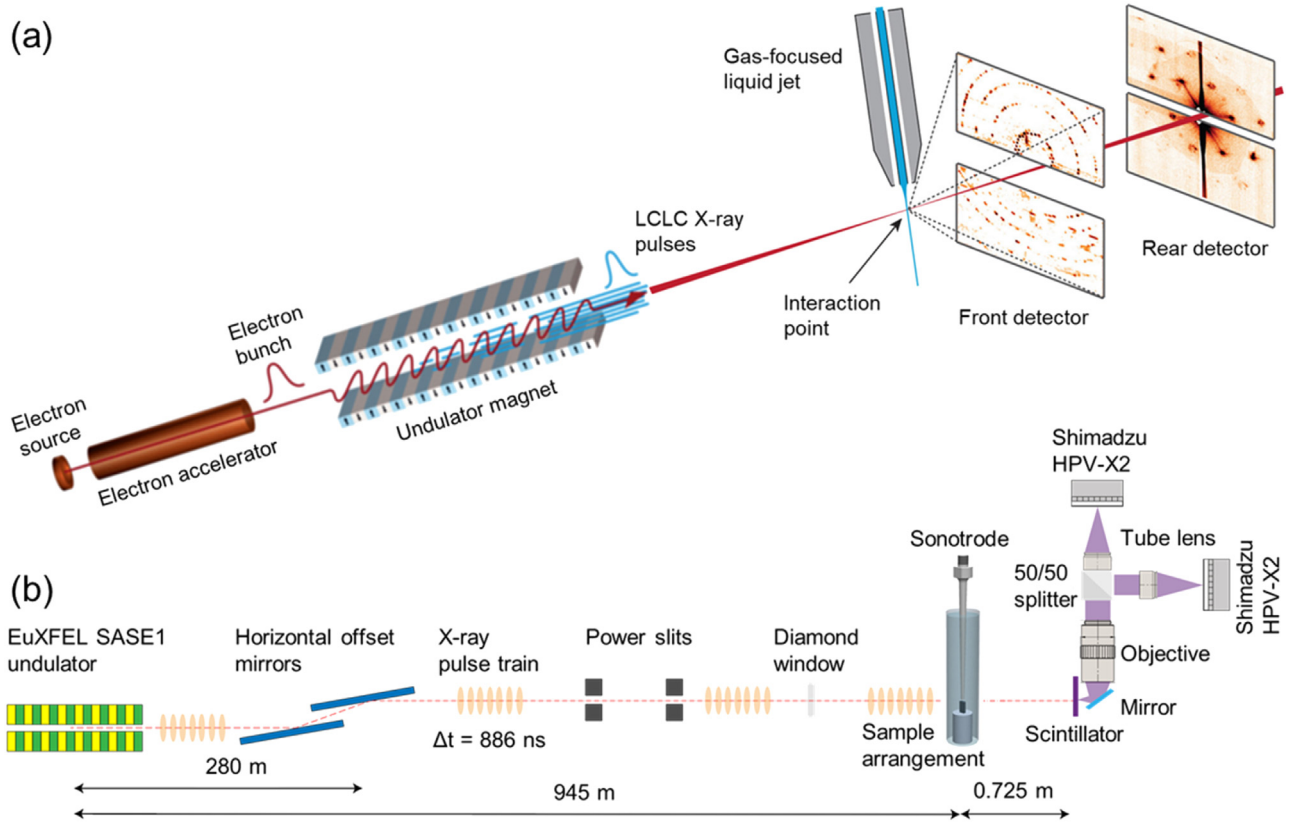


**Fig. 9.** (a) A schematic representation of X-ray pulses from the LCLS that are focused onto a continuously flowing microjet of crystals suspended in liquid [121]. (b) A schematic set-up of the world-first official XFEL megahertz imaging user experiment was conducted in September 2022 at the EuXFEL, studying the highly transient phenomena of ultrasonic cavitation dynamics with 25 fs exposure time per scan [122].

vantage of providing information with respect to the local atomic arrangement around a specific atomic species by examining the electronic transitions of inner shell electrons of a central atom [3,118]. By varying the incident X-ray energy across an absorption edge, the X-ray absorption near-edge structure (XANES) and extended X-ray absorption fine structure (EXAFS) are recorded. XANES yields information on the unoccupied valence states and the local geometry, while EXAFS provides structural details on the local environment around the X-ray absorber [114]. It can be applied in diverse external conditions, including variations in temperature, pressure, and more. It is not limited to crystalline materials but can also be used for amorphous systems, glasses, quasicrystals, disordered films, membranes, solutions, liquids, metalloproteins, and even molecular gases [119]. Fig. 8(c, d) shows that, by measuring the absorption cross-section of that element as a function of incident energy, valuable insights regarding the valence state and atomic configuration of the target element can be obtained. Therefore, XAFS is always an effective method no matter whether the atoms in the system are periodic or not [3].

#### 3.1.4. X-ray free-electron laser

In 2009, a new generation of X-ray sources commenced with the establishment of the Linac Coherent Light Source (LCLS) at Stanford. Fig. 7 compares the peak brightness as a function of photon energy between conventional lasers, synchrotron X-ray sources, and XFEL sources. As the first operational X-ray free-electron laser (XFEL) facility (Fig. 9), XFEL provides X-ray beams with peak brilliance approximately 10 orders of magnitude greater than the synchrotrons of the day [120].

The extremely high brightness enables time-resolved experiments in XFELs to capture the dynamics of chemical reactions, structural changes in materials, and biological processes [123]. In addition, it is able to produce trains of pulses with durations of a few fs to a few tens of fs, which is three orders of magnitude shorter than the pulse lengths produced by synchrotrons, allowing scientists to investigate ultrafast processes at the atomic and molecular levels [122,124].

However, currently, the most information that can be reliably extracted from an X-ray experiment from the isotropic glasses or liquid metals is the one-dimensional distribution function from which the three-dimensional structure cannot be directly generated. The X-ray data therefore represent an average overview of the structure from which only the first few peaks in the pair distribution function can typically be used to extract accurate atom-atom distances and coordination numbers [117].

### 3.2. Electron based techniques

Due to the lack of long-range order and transient movement of atoms in liquid metals, it is very challenging to conduct any sensible experimental investigation directly into the 3D atomic structure of liquid metals. In contrast, metallic glass is in a “frozen” state, maintaining an amorphous or non-crystalline structure due to the rapid cooling or quenching process. This stable solid state is “easier” for studying the local atomic structure. High-resolution transmission electron microscopy (HRTEM) is commonly used to investigate atomic structure, while such information is limited to two-dimensional representations [125].

In the past two decades, significant advancements have been made in the determination of the three-dimensional local structure of metallic glass. One is angstrom-beam electron diffraction (ABED), which was developed by Hirata et al. [126] in 2013. With

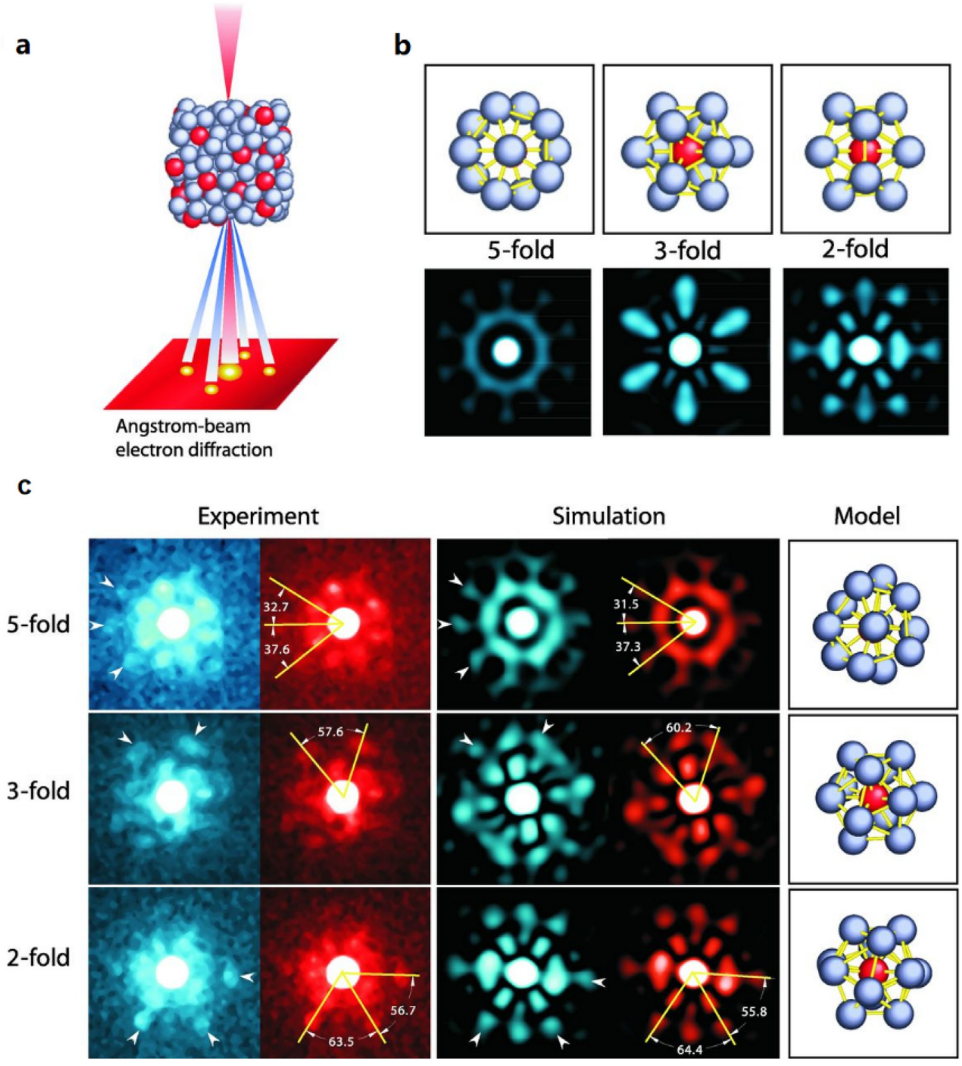


**Fig. 10.** ABED characterization of icosahedral order in metallic glasses [126]. (a) Experimental procedure of ABED of an icosahedral cluster. (b) Simulated ABED patterns of an ideal icosahedron. (c) Comparison between experimental and simulated ABED patterns of icosahedral clusters in a $Zr_{80}Pt_{20}$ metallic glass.

an electron beam of 0.36 nm diameter (see Fig. 10), they successfully captured diffraction patterns from sub-nm volumes within a metallic glass, which show some, but not all, of the expected features of an icosahedron [126].

In 2016, significant advances have been made in the field of atomic electron tomography (AET) led by Miao's group [127,128], enabling the precise determination of 3D structures of disordered systems at atomic resolution. Fig. 11 shows the schematic layout of AET. It illustrated that the reconstructed amorphous Ta film and Pd1 nanoparticle [106], with the real three-dimensional atomic structure, enables the precise identification and separation of crystalline atoms within the sample.

## 4. The modeling and simulation techniques

The structures and interatomic interactions in the liquid state can be described statistically by using the Pair Distribution Function (PDF) obtained from diffraction or absorption experiments. In 1988, the first PDF measurements were conducted to study the local structure of quasicrystals, initially with measurements using anomalous X-ray diffraction [130,131] and then neutron diffraction [132]. Since then, new diffractometers using (1) neutrons (2) synchrotron X-ray, and (3) electrons have been developed, providing opportunities for a deeper understanding of metallic materials' structures.

### 4.1. Pair distribution function

Fig. 12 shows a schematic illustration of how the total PDF is built up by finding atoms at a specific distance, $\boldsymbol{r}$, from the reference atom at the origin [133]. Depending on the research fields, sometimes, PDF is also called radial distribution function (RDF) or pair correlation function [134]. Normally, it takes three steps to get the $g(r)$ from a total scattering experiment. First, to obtain the raw scattering data via synchrotron or neutron experiments. Second, to reduce the raw data to obtain the structure factor $S(Q)$ ($Q$ is the wavevector). Finally, the PDF $g(r)$ can be obtained by the Fourier transform of $S(Q)$. PDFs have been widely used in many research fields in which different mathematic formulas were often used to emphasize particular physical features or structural characteristics [135].

The spatial resolution PDF is directly linked to the maximum value of $Q$, (i.e., $Q_{max}$) in scattering experiments. $Q_{max}$ is proportional to the maximum scattering angle and inversely proportional to the wavelength of the radiation used (usually $> 20$ Å$^{-1}$). Therefore, to achieve the largest possible $Q_{max}$ and attain maxi-

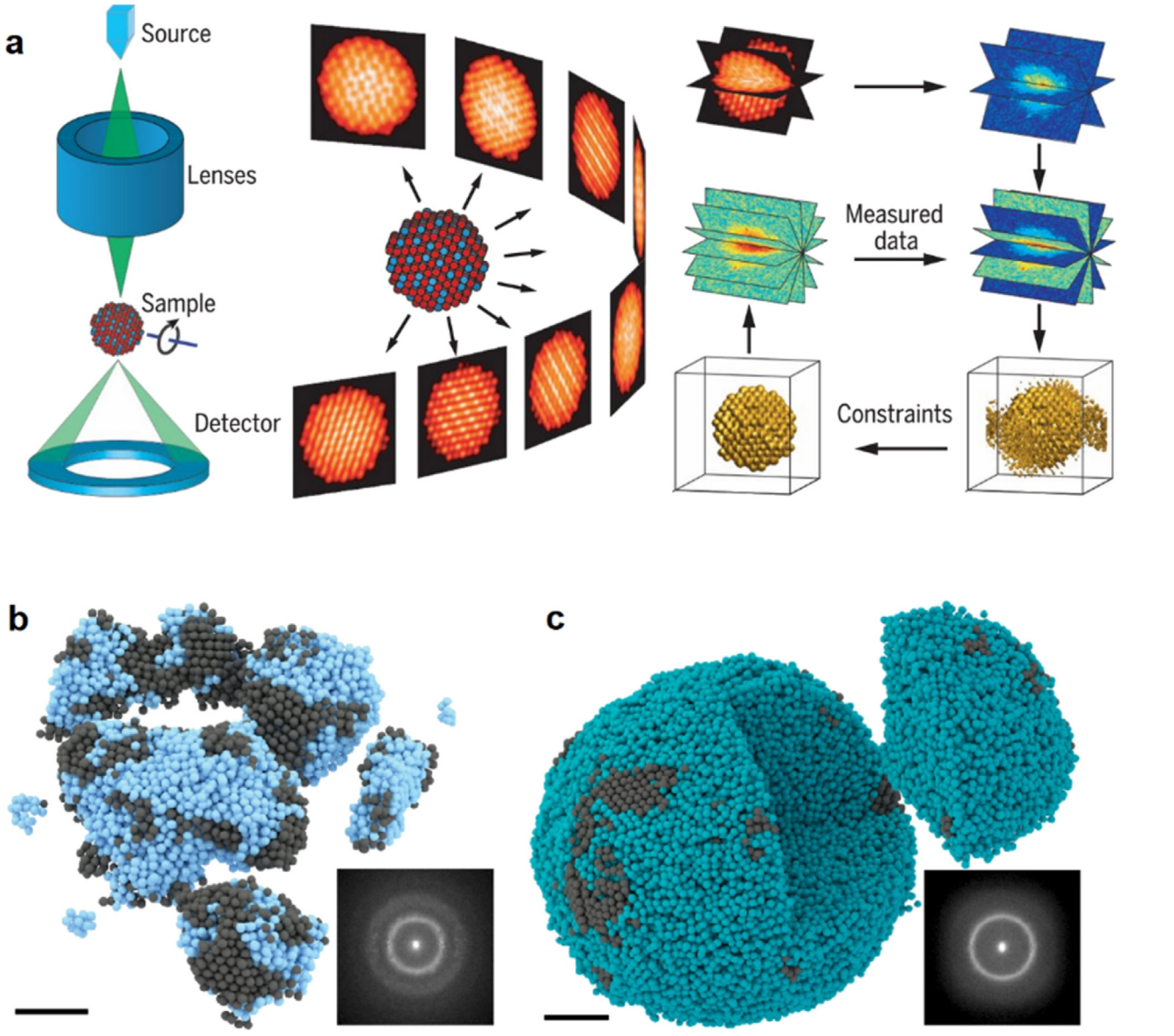


**Fig. 11.** (a) Schematic layout of AET [127]. Experimental 3D atomic model of an amorphous (b) Ta film (a) and a (c) $Pd_1$ nanoparticle [129] with surface crystal nuclei in grey. Scale bars: 2 nm.

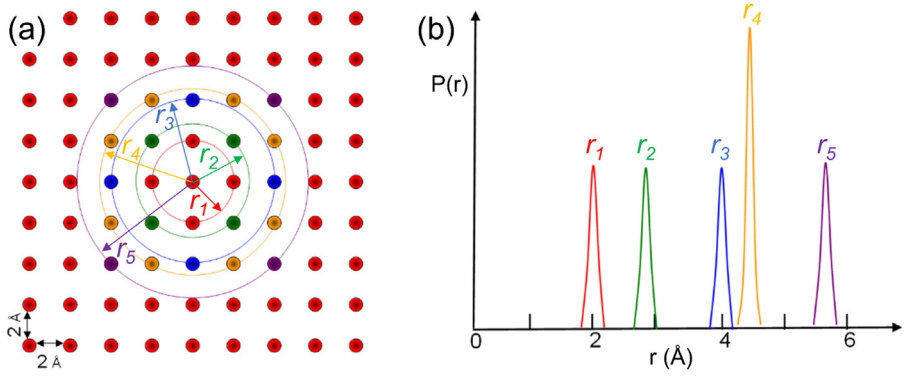


**Fig. 12.** A schematic illustration of how the total PDF is constructed by finding atoms at a distance, *r*, from the reference atom at the origin. (a) Circles indicate distances of neighboring atoms relevant to the reference atom in 2D view. (b) Corresponding peaks in the radial distribution function in the same color. The total PDF is obtained by repeating this process systematically by placing each atom at the origin [136].

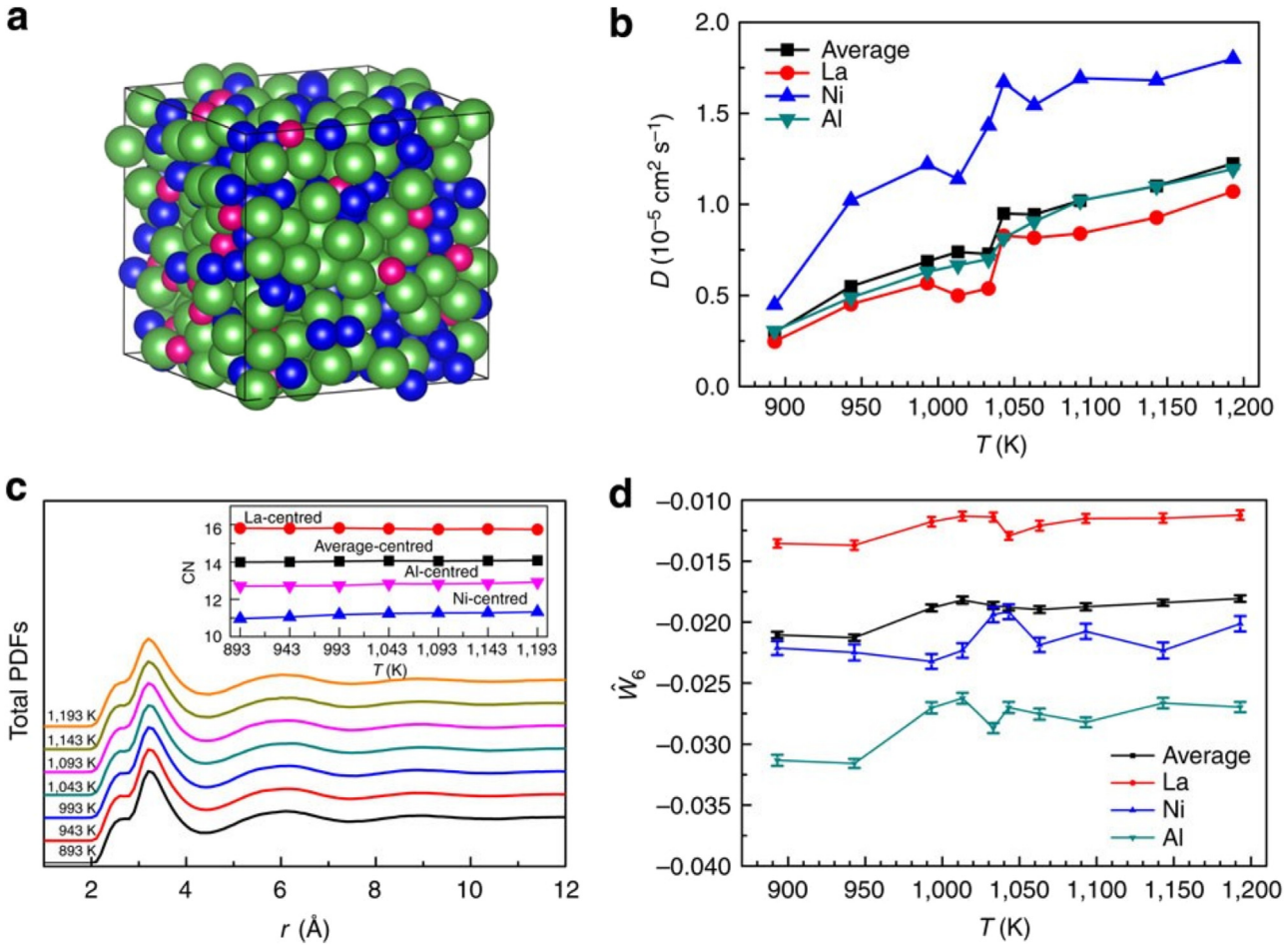


**Fig. 13.** (a) A typical atomic configuration equilibrated in the liquid state at 1143 K by AIMD simulation (La: green, Al: blue, and Ni: red). (b) Temperature-dependent diffusion coefficient (c) Total PDFs, coordination number, and (d) average $\hat{W}_6$ of all three elements and $\hat{W}_6$ of individual elements at different temperatures [157].

mum resolution in the PDF, total scattering experiments typically employ the shortest practicable radiation wavelength, usually less than or equal to 0.5 Å. Such short radiation wavelengths are readily available at neutron sources like Institut Laue–Langevin (ILL) in Grenoble, France, or ISIS in the UK, as well as at synchrotron X-ray sources (e.g., ESRF and DLS).

In PDF analysis, the structure of liquid is generally described in terms of two-body correlation functions, that is, the structure factors and the PDFs. The structure factor refers to the two-point correlation function of the microscopic density; the PDF refers to the two-point correlation function of variation of density as a function of distance from a reference particle. For the two-body correlation, the PDF technique can provide insights into the average interatomic distances, coordination environments, and certain structural features. On a microscopic level, particles in liquids can exhibit short- and medium-range order. The length scale of these two structural orderings can be quantified by the peak position analysis. Medium-range order (MRO), typically on a length scale of 5–10 Å, refers to structural ordering in amorphous systems beyond the nearest neighbor distances (SRO, typically within 5 Å) [137]. One of the most famous local structures directly revealed by PDF is the splitting of the second peak in the PDF, such phenomenon often indicates the appearance of local structure order in colloidal hard spheres and metallic glasses system [138]. Many researchers also found in the cooling process of liquid metal, the peak height of PDF always becomes higher, which is a sign that the liquid is becoming more and more ordered upon cooling [139].

### 4.2. Molecular dynamics modeling

Based on the experimentally measured data, several computational methods have been developed in the past 40 years to model or reconstruct the 3D atomic models [140,141]. In this aspect and relevant to this research field, the Reverse Monte Carlo (RMC) [142–144], Empirical Potential Structure Refinement (EPSR) [145,146], Density Function Theory (DFT), and *ab initio* Molecular Dynamics (AIMD) [99,103,147–151] methods have been widely used.

Currently, first-principle DFT and AIMD methods [152,153] are used to calculate the atomic configuration of binary or ternary metallic glasses or high-entropy alloys. However, the DFT method is difficult to deal with a system containing five or more elements, and the AIMD method is limited to small systems (normally a few hundred atoms) and a short period of time (~10–100 ps) [154]. Furthermore, although the RMC fitting method is often used to decouple the partial PDFs with large systems (several thousand atoms) [144], it does not have the physical meaning [155] and always runs into difficulties when attempting to decouple all partial PDFs in multi-component alloys. Only simulations of pure or binary alloy systems, e.g., Ni [71,100,101], Zr [156], $Cu_{50}Zr_{50}$ [156], and $Ni_{50}Al_{50}$ [103,156] were attempted to track such transition forming simple, stable BCC or FCC phases.

For example, Xu et al. [157] proposed the presence of an LLT in the glass-forming $La_{50}Al_{35}Ni_{15}$ melt (Fig. 13) above its liquidus temperature at 1143 K modeled by AIMD simulation. The

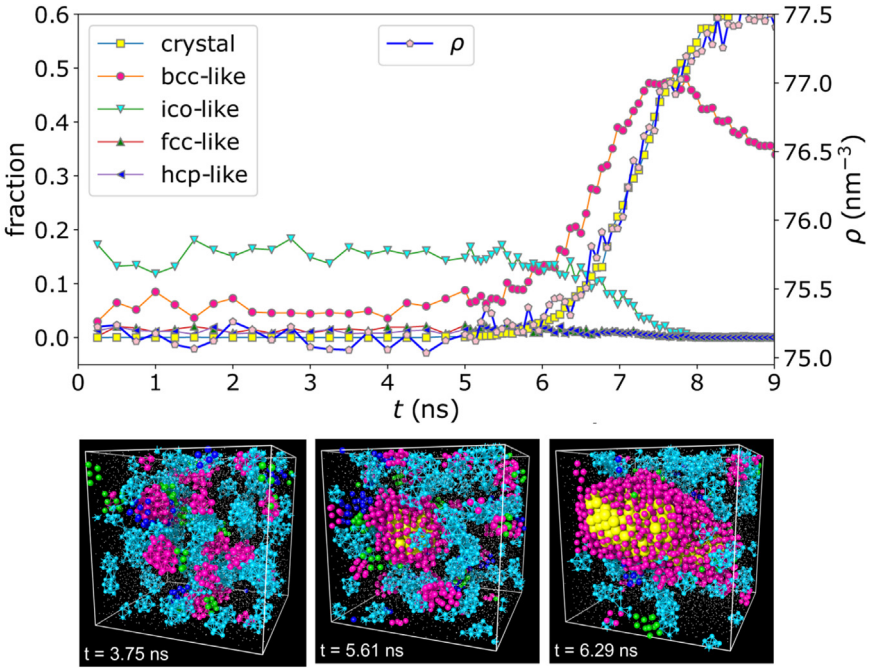


**Fig. 14.** The non-classical crystallization process of NiAl was revealed by molecular dynamics (MD) simulations [103].

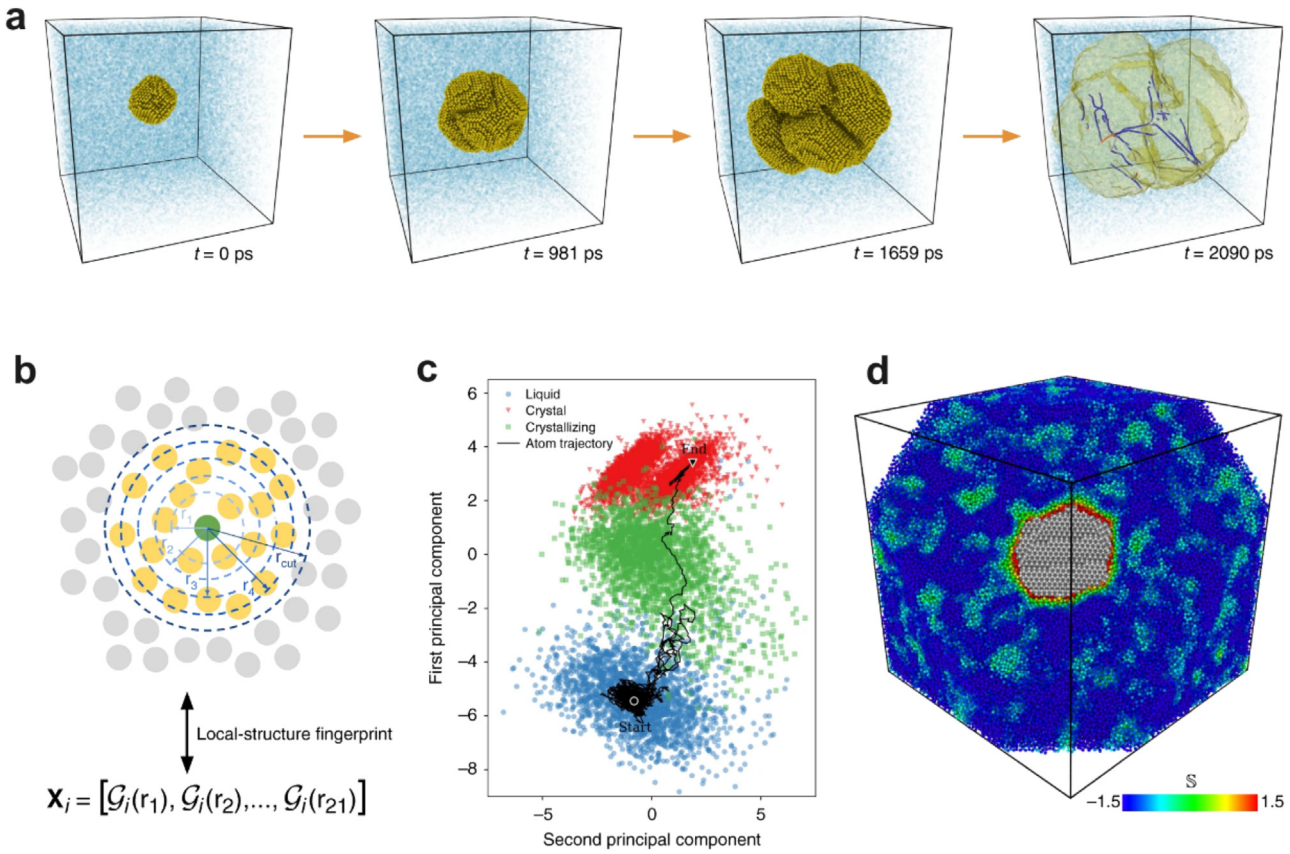


**Fig. 15.** (a) Snapshots of a crystal growth simulation of silicon using molecular dynamics. (b) The local structure (atoms in yellow) surrounding a central atom (green) is encoded using a set of 21 radial structure functions. (c) Atomic trajectory during crystallization as encoded by the time-evolution of local-structure fingerprints. (d) Cross section of a snapshot of the initial stages of silicon growth. Liquid atoms are colored according to their softness value [148].

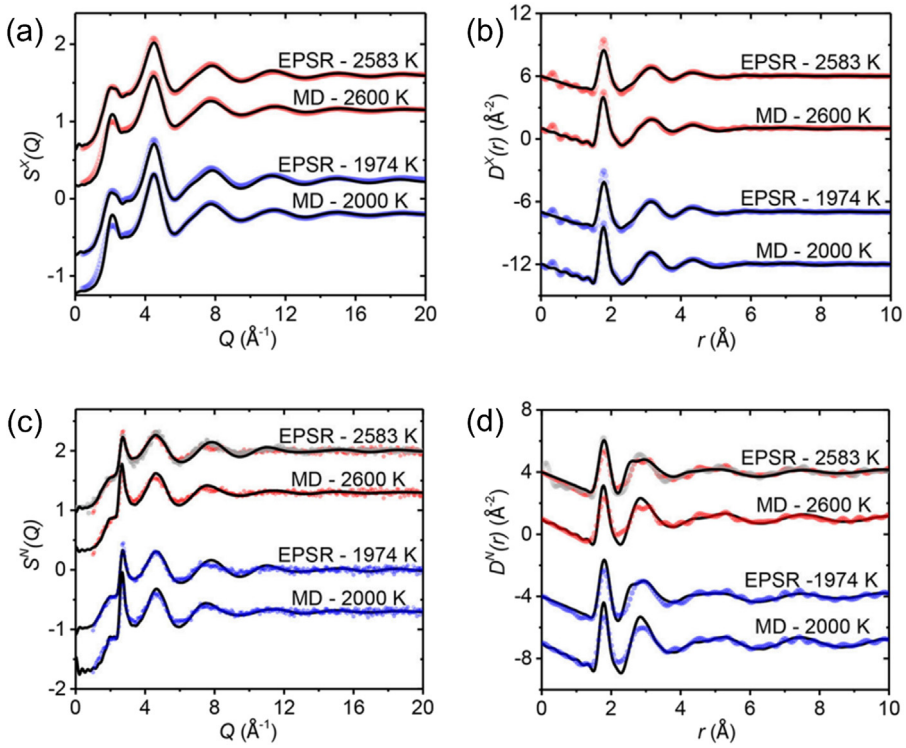


**Fig. 16.** The X-ray [159] (a, b) and neutron [160] (c, d) total structure factors $S(Q)$ (a, c) and total PDFs $D(r)$ (b, d) of liquid alumina ($D(r)$ is adopted to align with the original work), obtained with a $Q_{max}$ of 20.0 Å$^{-1}$. Each panel compares the measured data (points) to the EPSR and MD simulation results (solid black lines).

temperature-dependent diffusion coefficient of $La_{50}Al_{35}Ni_{15}$ liquid (Fig. 14(b)) shows qualitative changes around 1043 K. It can also be seen that the total PDFs and coordination numbers (Fig. 13(c)) do not show any noticeable change versus temperature, indicating that the change of density in the liquid metals varies very little over the investigated temperature range. Therefore, it can be concluded that the observed LLT in the present La-based alloy system is not a density-driven phase transition but bond orientational order change. Below 1050 K, the system goes through a temperature region where the individual $\hat{W}_6$ changes significantly until 1000 K (Fig. 13(d)).

Fig. 14 shows that in the liquid $Ni_{50}Al_{50}$, the stable B2 crystal phase forms in a non-classical nucleation pathway, where BCC-like pre-orders formed in the supercooled liquid share the same symmetry with the stable $B_2$ crystal phase, whereas the other crystal-like pre-orders (FCC-like and HCP-like) are negligible [103]. Freitas et al. [148] applied a machine learning-assisted MD method for the construction of a structural quantity (namely softness) that captures the propensity for atomic rearrangements to occur in disordered atomic environments. Fig. 15 shows strong spatial correlations and fluctuating heterogeneities in the reconstructed atomic structure, which have been found to be favorable locations for crystal nucleation according to recent studies [148,158].

In the EPSR method, the Lennard-Jones potentials plus Coulomb charge interactions are used as a starting reference potential, which captures the fact that atoms are not hard spheres and can be squashed up against each other (the $r^{12}$ part of the potential). In a longer range, the induction forces come from the correlated motion of the electrons in the system (the $r^6$ part of the potential). These potentials are the simple background interactions that allow the EPSR refinement to proceed, i.e., to move the position of the atoms in 3D space under a fixed bulk density of the system. On top of this, the empirical potential is then added as a perturbative force to capture the corrections that are required to put the positions of the atoms into agreement with the experimentally

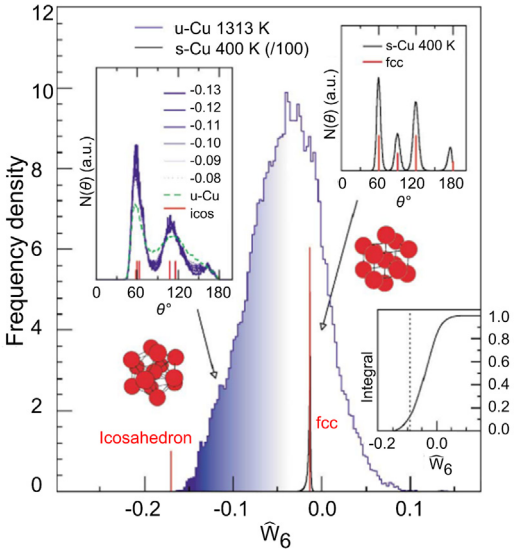


**Fig. 17.** Histogram of the frequency density of the $\hat{W}_6$ cubic invariant monitoring the local geometry around each atom in undercooled liquid Cu. The histogram related to the FCC solid Cu, limited to a very narrow region around –0.013161 (value for a "perfect" FCC 13-atom cluster), is shown for comparison (scaled by a factor of 100) [165].

determined atomic PDFs through the distance-dependent modifications to the interaction potentials. The EPSR simply aims to put the nuclear centers of the model atoms into positions consistent with the interpretation of neutron or X-ray scattering theory, one of the best understood and physically robust experimental tests that have been derived by modern science.

For example, Fig. 16 shows the comparison of the structural factors and PDFs of liquid Alumina at the selected temperatures obtained from synchrotron X-ray [159] and neutron [160] total scat-

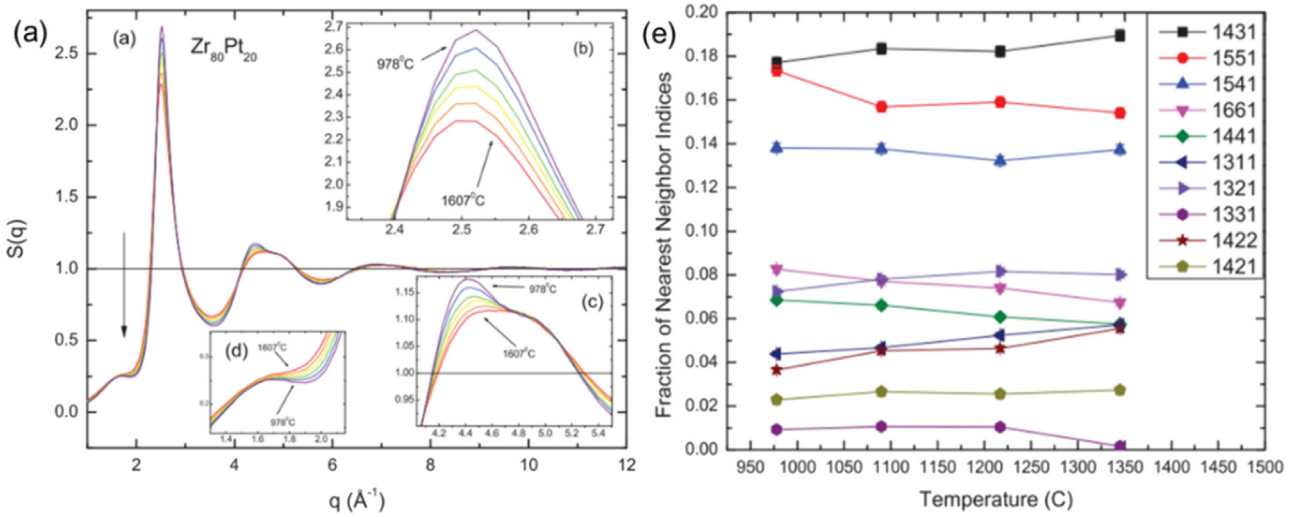


**Fig. 18.** (a) Static structure factor $S(q)$ for (a) Zr80Pt20 liquid at 1607, 1474, 1345, 1217, 1090, and 978 °C. The insets show the evolution of $S(q)$ with decreasing temperature for (b) the primary peak, (c) the second peak, and (d) the pre-peak (indicated with an arrow in the total structure factor). (e) The prominent Honeycutt and Andersen indices for the RMC liquid structure as a function of temperature, showing that all liquid structures are dominated by icosahedral (1551) and distorted icosahedral (1431 + 1541) order [167].

tering. The diffraction patterns have been fitted with EPSR models and compared to classical MD simulation results. Both EPSR and MD simulations reveal a direction of the temperature dependence of the aluminate network structure which moves further away from the glass-forming ideal during supercooling.

The scattered intensity of the structure factor from neutron and synchrotron differs a lot. In contrast, the modeled results by EPSR and molecular dynamics method agreed very well with the experimental data. In addition, other relatively new methods such as PDFFIT [161] and "Liga" [162] have been used in simulating nanostructured solids like C60 [163] and ferrihydrite [164] according to PDF data.

## 5. The research advances in different alloy systems

In 2003, Kelton's group [28] used *in-situ* synchrotron XRD measurements combined with the ESL technique at 6-ID-D of the APS to experimentally demonstrate for the first time that ISRO in the

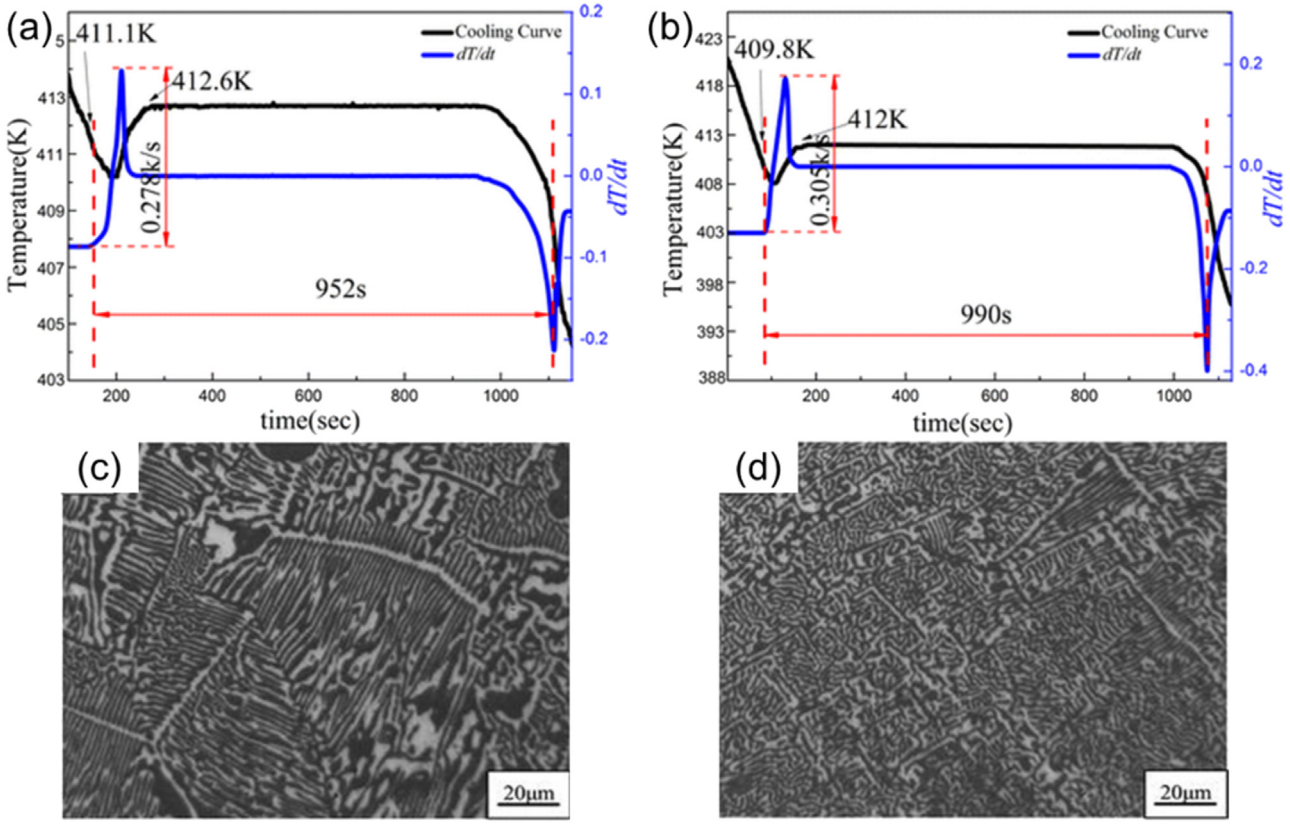


**Fig. 19.** The cooling curves and solidification structures of $Sn_{57}Bi_{43}$ alloy in (a, c) 30 min at 923 K; (b, d) 30 min at 1143 K [168].

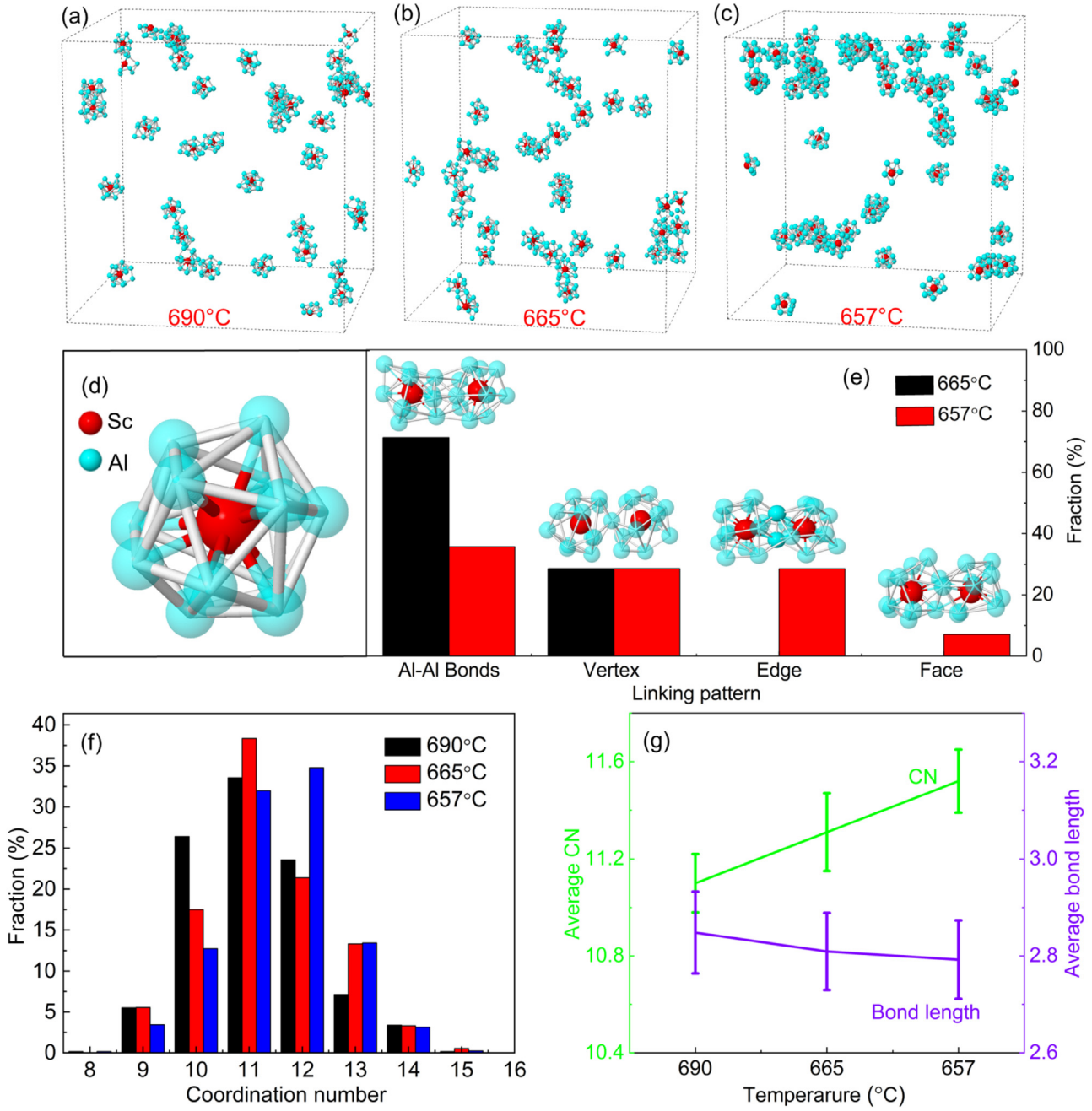


**Fig. 20.** The *Sc*-centred Al atom clusters in the Al-0.4Sc melt at (a) 690 °C, (b) 665 °C, and (c) 657 °C respectively extracted from the EPSR models. (d) An enlarged view of a *Sc*-centred Frank-Kasper polyhedron with a coordination number of 12 for the Al-0.4Sc melt at 690 °C. (e) Four different types of MROs formed by sharing the Al-Al bond, vertex, edge, and face between the neighboring clusters. (f) The coordination number distribution of the *Sc* atoms in the Al-0.4 *Sc* melts at 690, 665, and 657 °C respectively. (g) the average coordination number and average bond length of the Al-*Sc* atom pair as a function of temperature [170].

liquid and undercooled liquid metals, as well as its effects on the subsequent nucleation events. Since then, understanding the local atomic structure of liquid metals and their evolutions with temperature has been the central topic of metallurgical research. The key findings and most important progress made in numerous pure metals and metal alloy systems are described and discussed in this section.

### 5.1. Pure metals

In 2004, Lee et al. [29] studied the ISRO structures in undercooled pure liquid metals Ti and Ni using the same experimental technique as Kelton et al. [28]. The results show that although the SRO of liquid Ni was icosahedral, significantly distorted ISRO was observed in liquid Ti. This is the first experimental observation of distorted ISRO in liquid metals.

Cicco et al. [165] studied the local structure of liquid and undercooled liquid Cu using XAFS and theoretical simulation methods of undercooled Lennard-Jones liquids. The analyses show that the $\hat{W}_6$ distribution is very broad and includes a region (shaded area in Fig. 17) corresponding to distorted nearly icosahedral clusters, and the fraction of such configurations in undercooled Cu is about 10 %.

Xiong et al. [166] studied the temperature-dependent atomistic structure evolution of liquid gallium (Ga) using in situ high-energy XRD experiments and AIMD simulations. Both experimental and theoretical findings indicate a structural change in liq-

uid Ga around 1000 K. Below and above this temperature, the liquid exhibits variations in activation energy for self-diffusion, temperature-dependent heat capacity, coordination numbers, density, viscosity, electric resistivity, and thermoelectric power. They found that these variations are reflected in structural changes related to the bond-orientational order parameter $Q_6$, the fraction of covalent dimers averaged string length, and local atomic packing.

### 5.2. Binary metal systems

In 2011, Mauro et al. [167] studied the SROs and MROs in Zr80Pt20 liquid metals using the beamline ESL technique. The existence of a pre-peak at $q = 1.7$ Å$^{-1}$ in the structure factor of $Zr_{80}Pt_{20}$ liquids indicated MRO in the liquid. Besides, the MRO remained relatively unchanged with cooling (Fig. 18(d)). By using RMC simulation, they found that the pre-peak arose from a Pt-Pt correlation among Zr-centered clusters that had icosahedral and distorted-icosahedral symmetries. The icosahedral MROs differ significantly from the SROs observed in nucleating crystalline phases, responsible for elevating both interfacial energy and the nucleation barrier.

In 2016, Li et al. [168] investigated the effect of LLT on the microstructures of $Sn_{57}Bi_{43}$ alloy. They melt two samples in an electrical resistance furnace for 30 min at 923 K (sample A) and 1143 K (sample B), respectively. The results show that when solidifying from the melt experiencing the LLT, the melt structure transition can lead to a higher degree of undercooling, higher nucleation rate, and change of morphology (Fig. 19). The eutectic structure in $Sn_{57}Bi_{43}$ alloy is refined obviously, and the spacing of eutectic phase decreases obviously. They proposed that when the liquid experiences LLT, Sn-rich clusters start to either break up or disintegrate into smaller ones, and the nucleation of the phase Sn–Bi will be more difficult at high temperatures and will happen until a larger undercooling, which results in a higher nucleation rate and the refined Sn–Bi solidification structure. Additionally, after LLT, the melt has more consistent structures. This prompts eutectic phases to grow at lower temperatures [168]. Such refinement effects of solidification structures are also observed in Bi–Sb10 wt.% alloy in a similar manner [169].

In 2022, Huang et al. [170] studied the evolutions of 3D local atomic structures of the Al and an Al-0.4Sc alloy melts from liquid to liquid-solid coexisting state using synchrotron X-ray total scattering (SXTS) and EPSR modeling. Fig. 20 shows that, in the liquid state, ISRO *Sc*-centred Al polyhedrons form, and most of them with Al coordination number of 10–12. As the melt is cooled to a semisolid state, the polyhedrons become more connected atom clusters via vertex, edge, and face-sharing. These polyhedrons exhibit partially icosahedral and partially FCC symmetry. The MRO *Sc*-centred clusters with face-sharing are proved to be the "precursors" for the $Al_3Sc$ phases in the liquid-solid coexisting state.

In the same year, Li's group [171] investigated the local atomic structure of Al-Ni, Al-Bi [172], Al-Cu-La [173], and Al-Zn-Cr [174] alloy systems above the liquidus temperature using high-energy synchrotron XRD in the beamline BL13W1 of SSRF, coupled with

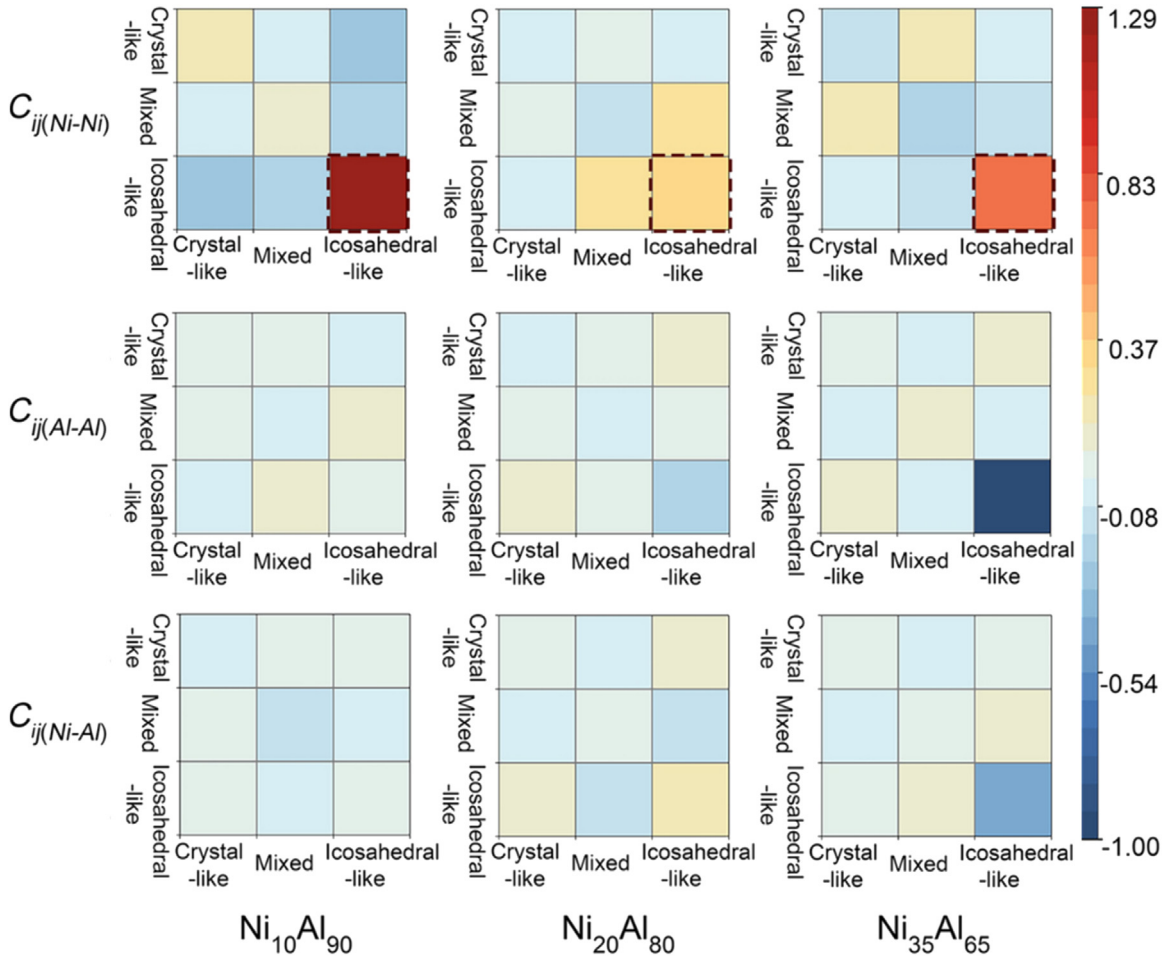


**Fig. 21.** The matrix of spatial correlation index $C_{ij}$ of three types (crystal-like, mixed, and icosahedral-like) clusters. $C_{ij}$ includes $C_{ij(Ni\text{–}Ni)}$, $C_{ij(Al\text{–}Al)}$, and $C_{ij(Al\text{–}Ni)}$ of the investigated liquids at 9 °C above the liquidus temperature [171].

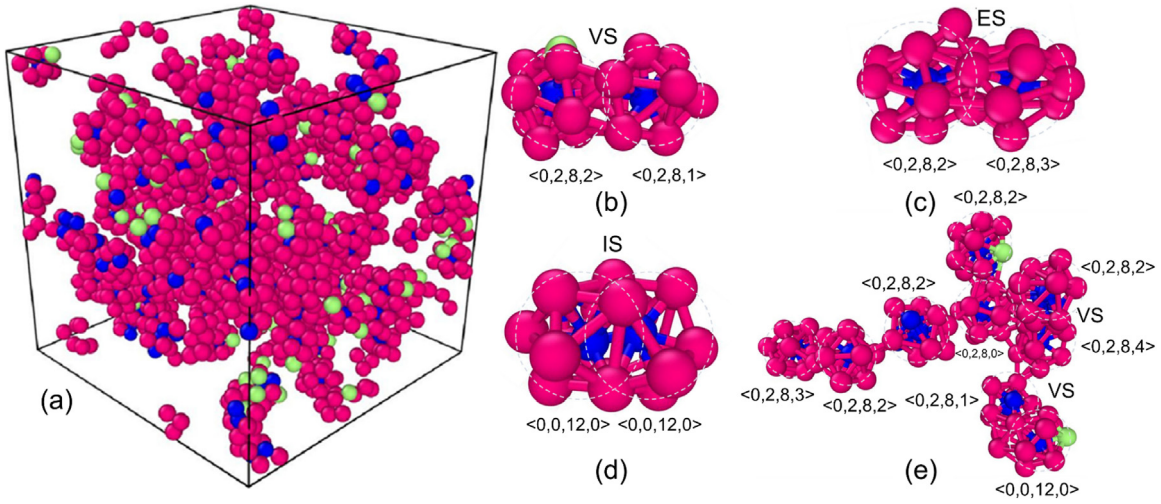


**Fig. 22.** (a) Snapshots of the spatial distribution around Cr atoms in an Al-20Zn-10Cr alloy at the temperature of 15 °C above the liquidus. The red, green, and blue circles represent Al, Zn, and Cr atoms, respectively. Extended icosahedral clusters linked by (b) vertex-, (c) edge-, and (d) intercross-shared atoms. (e) IMRO structure is composed of 1 perfect icosahedral and 7 icosahedral-like clusters. It contains 96 Al, 2 Zn, and 15 Cr atoms, which results in a local composition of $Al_{84.96}Zn_{1.77}Cr_{13.27}$, which is close to the $Al_{45}Cr_7$ intermetallic phase with several five-fold symmetry [174].

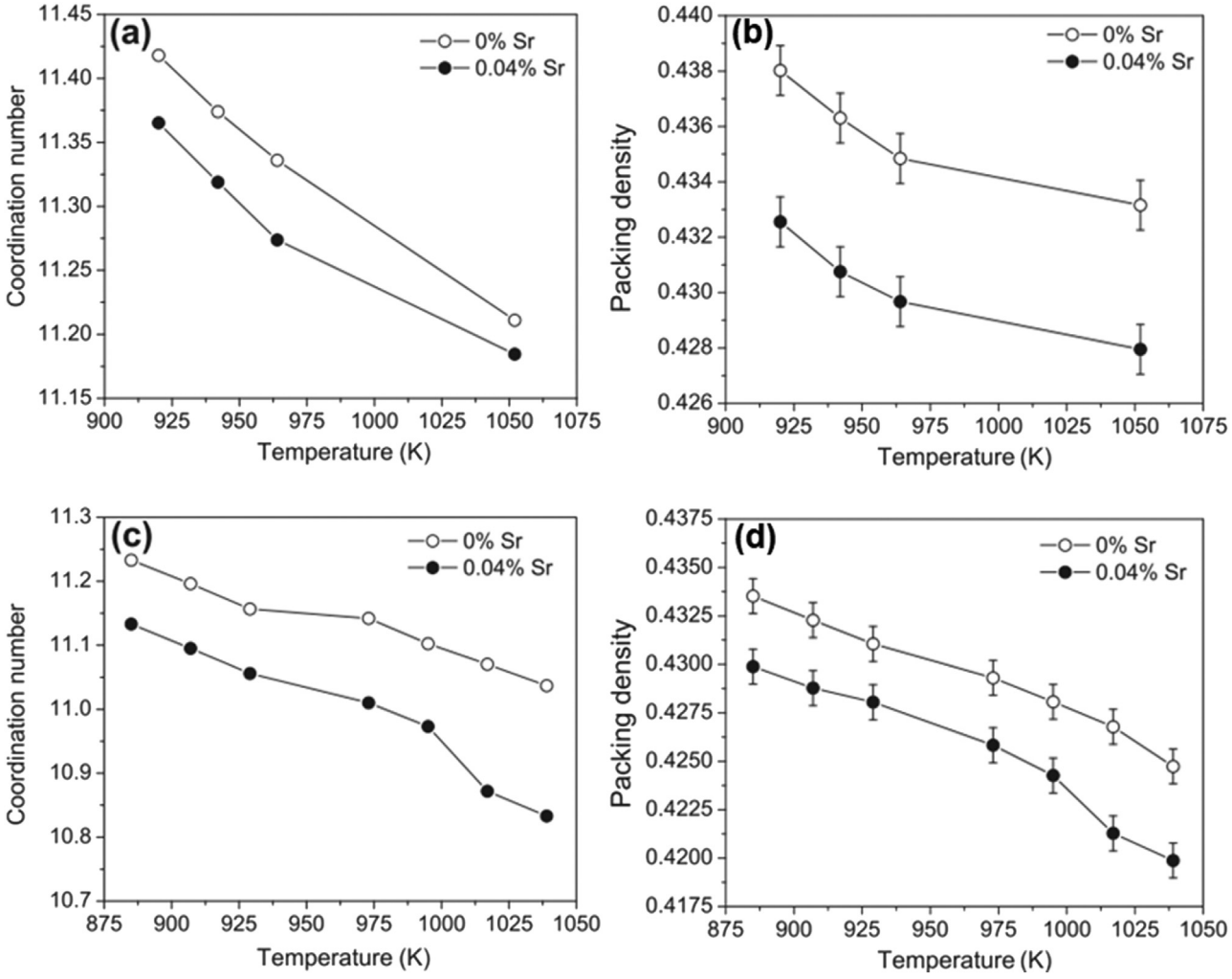


**Fig. 23.** (a, c) Coordination number variation with the addition of Sr in Al-3 %Si and Al-10 %Si alloy as a function of melting temperature. (b, d) Liquid atomic packing density variation with the addition of Sr in Al-3 %Si and Al-10 %Si alloys at various melt temperatures [175].

RMC and AIMD simulations. For example, in the Al-Ni alloy system, they observed a strong interconnection of central atoms among the Ni-Ni icosahedral-like clusters in the $Ni_{10}Al_{90}$, $Ni_{20}Al_{80}$, and $Ni_{35}Al_{65}$ (at%) alloy liquids (marked as black dot rectangles in Fig. 21), stimulating the intermetallic formation.

### 5.3. Ternary metal systems

While in the Al-Zn-Cr alloy system, adding Cr is found to hinder the formation of Al-centered ISRO and enhance the formation of Zn-centered ISRO. Abundant ISRO or patterns with high five-fold symmetry are observed around the chromium atoms. Additionally, the spatial correlation between Al and Zn atoms undergoes a substantial change due to the addition of chromium. Al- and Cr-centered with five-fold symmetry strongly tend to aggregate together to form MROs. Fig. 22 shows that, through the linkage of vertex-, edge- and intercross-shared types of the Cr-centered icosahedra or icosahedra-like clusters the icosahedral MRO are formed in the liquids, which have similar compositions to the $Al_{45}Cr_7$ intermetallic phase, and therefore are considered to be precursors for nucleation in the subsequent cooling. These findings may provide structural hints of the quasicrystal-enhanced nucleation mechanism.

Besides, Srirangam et al. [175] studied the effects of the addition of 0.04 wt.% Sr on the liquid structures of Al-Si alloys in 2011. Fig. 23 shows that, with the addition of Sr in the liquid alloys, the atomic coordination number and packing density increase with decreasing temperature and decreasing Si content of the alloy. Additionally, adding strontium (Sr) to these alloys delays or hinders atom clustering near nucleation temperatures. This is more pronounced in the eutectic alloy, which forms inter-dendritic liquid compositions during the final stages of solidification. When Sr is added to the eutectic alloy, insufficient atom clustering at the eutectic temperature may result in undercooling of the inter-dendritic liquid. This triggers the spontaneous crystallization of the Si phase on the primary Al phases, acting as heat sinks during the solidification process.

### 5.4. Multi-component metal systems

For multi-component alloys, understanding of how complex phases are nucleated in a multicomponent liquid (or semi liquid) is still a great challenge. The complexity and dynamic coupling among the multiple elements increases drastically for simulation and for experiments. Affinities between different chemical species must be considered carefully since they induce multiple different chemical orders and stabilize complex solid phases.

In 2023, Huang et al. [176] studied the atomic structures of multi-component Al-5Cu-1.5Fe-1Si alloy system in the liquid state and their dynamic evolution versus temperature by combining synchrotron X-ray total scattering and EPSR modeling methods. Fig. 24(a) shows three typical Fe-centred superclusters extracted from the simulation box of the 3 alloy melts. The superclusters are connected with the Fe-centered SRO via five different connection modes, which are by sharing the Al-Al bonds (BS), vertex (VS), edge (ES), face (FS), and tetrahedra (TS) between the neighboring clusters. Clearly, the BS is the main connection mode in all 3 melts. Fig. 24(c) reveals that the fraction of Fe-centred MROs con-

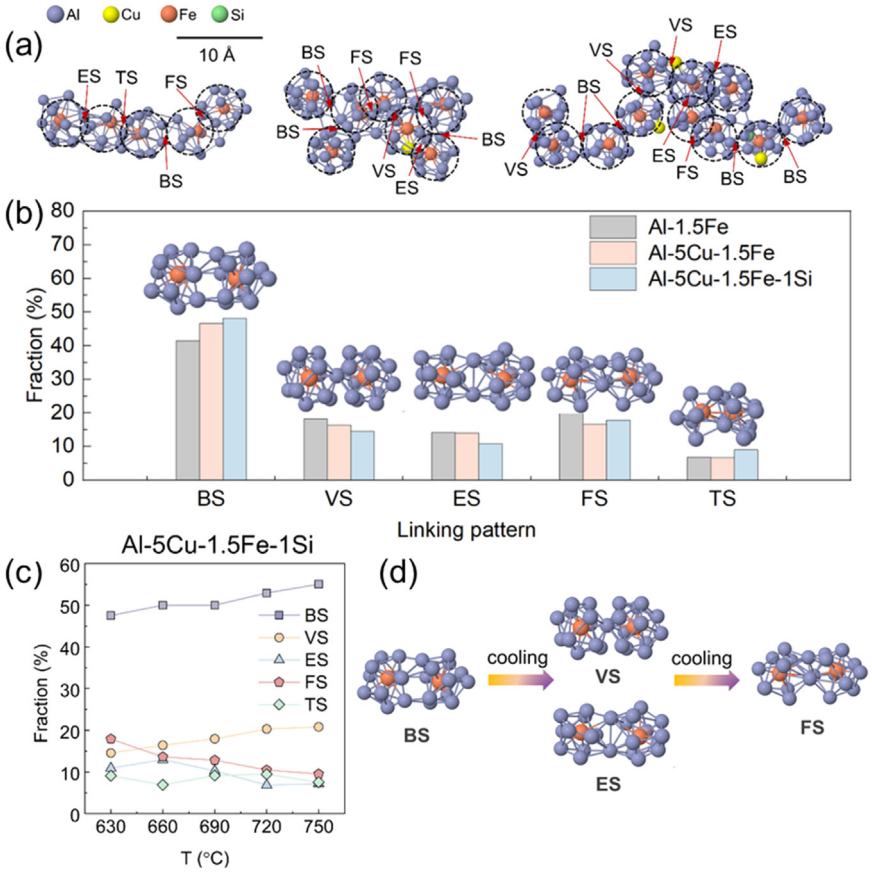


**Fig. 24.** (a) Three typical Fe-centred superclusters in the Al-5Cu-1.5Fe-1Si alloy liquid. (b) The corresponding fractions of the five connection modes for the Fe-centred MROs in Al-1.5Fe, Al-5Cu-1.5Fe, and Al-5Cu-1.5Fe-1Si alloys prior to crystallization (750–632 °C). The insets show the 3D configuration of the Fe-centred MROs constructed by different connection modes. (c) Variation of different supercluster connection modes of Al-5Cu-1.5Fe-1Si alloys versus temperature during the cooling process. (d) A schematic of Fe-centred MROs evolution pathway [176].

nected by BS decreases, while both ES and FS increase gradually during cooling. This phenomenon indicates that during the cooling process, the Fe-centred MROs become more compact, resulting in gradual changes in the connection modes. Therefore, the author proposed one possible transition pathway that the BS-connected MROs evolve into those connected by VS and ES, and then into the MROs connected by FS. Finally, the multiple Fe-centred clusters linked by the FS connection with the nearest Fe atoms will act as precursors for nucleation of the monoclinic $Al_{13}Fe_4$ phase. Hence the crystal nucleation starts with the formation of MRO clusters with similar structures to the subsequently nucleated crystal.

## 6. Summary and outlook

In summary, in the past 30 years or so and since the development and wide availability of the powerful synchrotron X-rays, research on studying the liquid metal atomic structures has been accelerated and major advances have been made in elucidating heterogeneous structures in bulk liquid, liquid surface, and liquid-solid interfaces for numerous pure metals and metal alloys systems. Combining the advanced Synchrotron X-ray experimental techniques and suitable molecular dynamic modeling methods, high-fidelity 3D liquid metal atomic structures can be built that agree well with the experimental measurement. However, difficulties and challenging scientific issues remained, for example, direct experimental observations of the structural heterogeneity in a superheated, non-equilibrium, and fast cooling condition are still very difficult. It is very challenging to track experimentally and retrieve real-time dynamic evolution of the intermediate states of atomic structures and how they facilitate the onset of crystal nucleation especially in undercooled conditions. This is mainly due to the required atomic-scale spatial resolution and the ns-fs second-time resolution for the probing beams and the associated detectors. In this aspect, the exceptionally high brightness of the XFEL is an ideal source for exploring time-resolved experiments with time resolution of tens of femtoseconds. Using XFEL, it is possible to image phase nucleation from femtosecond onwards, obtaining the missing data at the critical liquid-solid phase nucleation processes [120]. For resolving the 3D atomic structures of multiple-component alloys, complementary simulation and modelling methods (i.e., DFT, AIMD, and EPSR) need to be used. Simulation and modeling need to be run with a much larger simulation box that can handle and process hundreds of thousands of atoms or even millions of atoms in order to approach the reality. Recently, the ISIS team has just made Dissolve (a new code based on the EPSR) available for users to simulate ever-increasing complex systems with heterogeneous structures. Dissolve employs a full classical force field and can accommodate multi-configuration simulations with millions of atoms. In companying with the fast advance in high-performance computing and computational materials science. Research in this field will advance at a speed never seen before, resolving the long-standing scientific and technological issues in this field in the foreseeable future.

## Declaration of competing interest

I declare that there is no conflict of interest among all authors concerning the submitted manuscript.

## Acknowledgements

We would like to acknowledge the funding and financial support given by the UK Engineering and Physical Science Research Council (No. EP/L019965/1). Kang Xiang and Shi Huang would also like to acknowledge the financial support from the University of Hull and China Scholarship Council for their PhD studies at the University of Hull.

## References

[1] D.L. Goodstein, States of Matter, Dover Publications, Garden City, USA, 2014.
[2] J.A. Barker, D. Henderson, Rev. Mod. Phys. 48 (1976) 587.
[3] Y. He, J. Li, J. Wang, E. Beaugnon, Trans. Nonferrous Met. Soc. China 30 (2020) 2293–2310.
[4] L. Qin, W. Du, S. Cipiccia, A.J. Bodey, C. Rau, J. Mi, Acta Mater. 265 (2023) 119593.
[5] B. Wang, D. Tan, T.L. Lee, J.C. Khong, F. Wang, D. Eskin, T. Connolley, K. Fezzaa, J. Mi, Acta Mater. 144 (2018) 505–515.
[6] C.J. Smithells, Metals Reference Book, Elsevier, Amsterdam, Netherlands, 2013.
[7] J.M. Dmitry, G. Eskin, Solidification Processing of Metallic Alloys Under External Fields, Springer International Publishing, Cham, Switzerland, 2018.
[8] A. Mühlbauer, History of Induction Heating and Melting, Vulkan-Verlag GmbH, Essen, Germany, 2008.
[9] P.G. Debenedetti, Metastable liquids: Concepts and Principles, Princeton University Press, USA, 1996.
[10] I.G.e. Brodova, P.S. Popel, G.I. Eskin, Liquid Metal processing: Applications to Aluminium Alloy Production, CRC Press, Boca Raton, USA, 2001.
[11] A.R.J.P. Ubbelohde, Proc. R. Soc. London Ser. A-Math. Phys. Eng. Sci. 293 (1966) 291–309.
[12] T. Ishikawa, P.F. Paradis, T. Itami, S. Yoda, Meas. Sci. Technol. 16 (2005) 443.
[13] J.R. Weber, S. Krishnan, P.C. Nordine, JOM 43 (1991) 8–14.
[14] I. Egry, D. Holland-Moritz, Levitation methods for structural and dynamical studies of liquids at high temperatures, Eur. Phys. J. Spec. Top. 196 (2011) 131–150.
[15] D.L. Price, High-temperature Levitated Materials, Cambridge University Press, UK, 2010.
[16] E. Brandt, Science 243 (1989) 349–355.
[17] L. Hennet, V. Cristiglio, J. Kozaily, I. Pozdnyakova, H. Fischer, A. Bytchkov, J. Drewitt, M. Leydier, D. Thiaudière, S. Gruner, Eur. Phys. J. Spec. Top. 196 (2011) 151–165.
[18] P.C. Nordine, R.M. Atkins, Rev. Sci. Instrum. 53 (1982) 1456–1464.
[19] J.K. Weber, A. Tamalonis, C.J. Benmore, O.L. Alderman, S. Sendelbach, A. Hebden, M.A. Williamson, Rev. Sci. Instrum. 87 (2016) 073902.
[20] J.K.R. Weber, C.J. Benmore, L.B. Skinner, J. Neuefeind, S.K. Tumber, G. Jennings, L.J. Santodonato, D. Jin, J. Du, J.B. Parise, J. Non-Cryst. Solids 383 (2014) 49–51.
[21] K. Beard, H. Pruppacher, J. Atmos. Sci. 26 (1969) 1066–1072.
[22] C. Benmore, J. Weber, Adv. Phys.-X 2 (2017) 717–736.
[23] T. Schenk, D. Holland-Moritz, V. Simonet, R. Bellissent, D.M. Herlach, Phys. Rev. Lett. 89 (2002) 075507.
[24] E. Laithwaite, Proc. Instit. Electr. Eng. 112 (1965) 2361–2375.
[25] G. Jacobs, I. Egry, Phys. Rev. B 59 (1999) 3961.
[26] G. Jacobs, I. Egry, D. Holland-Moritz, D. Platzek, J. Non-Cryst. Solids 232–234 (1998) 396–402.
[27] K.F. Kelton, G.W. Lee, A.K. Gangopadhyay, R.W. Hyers, T.J. Rathz, J.R. Rogers, M.B. Robinson, D.S. Robinson, Phys. Rev. Lett. 90 (2003) 195504.
[28] G.W. Lee, A.K. Gangopadhyay, K.F. Kelton, R.W. Hyers, T.J. Rathz, J.R. Rogers, D.S. Robinson, Phys. Rev. Lett. 93 (2004) 037802.
[29] A.K. Gangopadhyay, G.W. Lee, K.F. Kelton, J.R. Rogers, A.I. Goldman, D.S. Robinson, T.J. Rathz, R.W. Hyers, Rev. Sci. Instrum. 76 (2005) 073901.
[30] T. Kordel, D. Holland-Moritz, F. Yang, J. Peters, T. Unruh, T. Hansen, A. Meyer, Phys. Rev. B 83 (2011) 104205.
[31] N.A. Mauro, K.F. Kelton, Rev. Sci. Instrum. 82 (2011) 035114.
[32] W.K. Rhim, S.K. Chung, D. Barber, K.F. Man, G. Gutt, A. Rulison, R.E. Spjut, Rev. Sci. Instrum. 64 (1993) 2961–2970.
[33] C.J. Benmore, J.K.R. Weber, Phys. Rev. X 1 (2011) 011004.
[34] J. Leiterer, W. Leitenberger, F. Emmerling, A.F. Thünemann, U. Panne, J. Appl. Crystallogr. 39 (2006) 771–773.
[35] W. Mirihanage, D. Browne, G. Zimmermann, L. Sturz, Acta Mater. 60 (2012) 6362–6371.
[36] H. Nguyen-Thi, G. Reinhart, B. Billia, C.R. Mec. 345 (2017) 66–77.
[37] L. Hennet, D.H. Moritz, R. Weber, A. Meyer, in: High-temperature Levitated materials, Experimental methods in the Physical Sciences, Elsevier, Amsterdam, Netherlands, 2017, pp. 583–636.
[38] S. Spitans, E. Baake, B. Nacke, A. Jakovičs, Magnetohydrodynamics 51 (2015) 121–132.
[39] A. SALLES, Lasers, levitation and machine learning make better heat-resistant materials. https://www.anl.gov/article/lasers-levitation-and-machine-learning-make-better-heatresistant-materials.
[40] E. Okress, D. Wroughton, G. Comenetz, P. Brace, J. Kelly, J. Appl. Phys. 23 (1952) 545–552.
[41] H. Weis, D. Holland-Moritz, F. Kargl, F. Yang, T. Unruh, T. Hansen, J. Bednarčik, A. Meyer, Phys. Rev. B 104 (2021) 134108.
[42] S. Stüber, D. Holland-Moritz, T. Unruh, A. Meyer, Phys. Rev. B 81 (2010) 024204.
[43] S.M. Chathoth, A. Meyer, M. Koza, F. Juranyi, Appl. Phys. Lett. 85 (2004) 4881–4883.
[44] P.F. Paradis, T. Ishikawa, G.W. Lee, D. Holland-Moritz, J. Brillo, W.K. Rhim, J.T. Okada, Mater. Sci. Eng. R-Rep. 76 (2014) 1–53.
[45] C.E.P. Talbot, N.L. Church, E.M. Hildyard, L.D. Connor, J.R. Miller, N.G. Jones, Acta Mater. 262 (2024) 119409.

[46] S. Kohara, M. Itou, K. Suzuya, Y. Inamura, Y. Sakurai, Y. Ohishi, M. Takata, J. Phys.-Condes. Matter 19 (2007) 506101.
[47] K. Bücks, H. Müller, Z. Phys. 84 (1933) 75–86.
[48] H.W.S. Clair, Ind. Eng. Chem. 41 (1949) 2434–2438.
[49] E. Trinh, Rev. Sci. Instrum. 56 (1985) 2059–2065.
[50] J.J.-Z. Li, Study of Liquid Metals By Electrostatic Levitation, California Institute of Technology, 2009 Ph.D. Thesis.
[51] N. Mauro, J. Bendert, A. Vogt, J. Gewin, K. Kelton, J. Chem. Phys. 135 (2011) 044502.
[52] H. Tostmann, E. DiMasi, P.S. Pershan, B.M. Ocko, O.G. Shpyrko, M. Deutsch, Phys. Rev. B 59 (1999) 783–791.
[53] E. Dimasi, H. Tostmann, Synchrot. Radiat. News 12 (1999) 41–46.
[54] S. Oh, Y. Kauffmann, C. Scheu, W. Kaplan, M. Ruhle, Science 310 (2005) 661–663.
[55] M. Gandman, Y. Kauffmann, C.T. Koch, W.D. Kaplan, Phys. Rev. Lett. 110 (2013) 086106.
[56] L. Wang, W. Lu, Q. Hu, M. Xia, Y. Wang, J.G. Li, Acta Mater. 139 (2017) 75–85.
[57] Z. Ding, Q. Hu, W. Lu, S. Sun, M. Xia, J. Li, Scr. Mater. 130 (2017) 214–218.
[58] X. Li, F. Zu, J. Yu, B. Zhou, Phase Transit. 81 (2008) 43–50.
[59] G. Lee, A. Gangopadhyay, T. Croat, T. Rathz, R. Hyers, J. Rogers, K. Kelton, Phys. Rev. B 72 (2005) 174107.
[60] D. Holland-Moritz, D. Herlach, K. Urban, Phys. Rev. Lett. 71 (1993) 1196.
[61] M. Leocmach, H. Tanaka, Nat. Commun. 3 (2012) 1–8.
[62] E.R. Weeks, D. Weitz, Phys. Rev. Lett. 89 (2002) 095704.
[63] J. Conrad, F.W. Starr, D. Weitz, J. Phys. Chem. B 109 (2005) 21235–21240.
[64] C. Patrick Royall, S.R. Williams, T. Ohtsuka, H. Tanaka, Nat. Mater. 7 (2008) 556–561.
[65] S. Jeon, T. Heo, S.Y. Hwang, J. Ciston, K.C. Bustillo, B.W. Reed, J. Ham, S. Kang, S. Kim, J. Lim, Science 371 (2021) 498–503.
[66] T. Kawasaki, H. Tanaka, J. Phys.-Condes. Matter 22 (2010) 232102.
[67] A. Widmer-Cooper, P. Harrowell, Phys. Rev. Lett. 96 (2006) 185701.
[68] C. Brito, M. Wyart, J. Chem. Phys. 131 (2009) 149.
[69] T. Speck, A. Malins, C.P. Royall, Phys. Rev. Lett. 109 (2012) 195703.
[70] G.D. Leines, A. Michaelides, J. Rogal, Faraday Discuss 235 (2022) 406–415.
[71] J. Taffs, C.Patrick Royall, Nat. Commun. 7 (2016) 1–7.
[72] Y. Cheng, E. Ma, Prog. Mater. Sci. 56 (2011) 379–473.
[73] T. Kawasaki, H. Tanaka, Proc. Natl. Acad. Sci. 107 (2010) 14036–14041.
[74] L. Wang, X. Bian, J. Liu, Phys. Lett. A 326 (2004) 429–435.
[75] X. Qiu, J. Li, J. Wang, T. Guo, H. Kou, E. Beaugnon, Mater. Chem. Phys. 170 (2016) 261–265.
[76] F.Q. Zu, Z.G. Zhu, L.J. Guo, X.B. Qin, H. Yang, W.J. Shan, Phys. Rev. Lett. 89 (2002) 125505.
[77] J. Hou, H. Guo, J. Sun, X. Tian, C. Zhan, X. Qin, X. Chen, Phys. Lett. A 358 (2006) 171–175.
[78] J. Wang, J. Li, R. Hu, H. Kou, E. Beaugnon, Mater. Lett. 145 (2015) 261–263.
[79] X. Li, F. Zu, W. Gao, X. Cui, L. Wang, G. Ding, Appl. Surf. Sci. 258 (2012) 5677–5682.
[80] S. Golde, T. Palberg, H.J. Schöpe, Nat. Phys. 12 (2016) 712–717.
[81] A. Arav, Y. Natan, Transfus. Med. Hemother. 46 (2019) 182–187.
[82] B.J. Luyet, M.P. Gehenio, Biodynamica 3 (1940) 33–39.
[83] B.J. Luyet, E.L. Hodapp, Proc. Soc. Exp. Biol. Med. 39 (1938) 433–434.
[84] A.M. Kaushal, P. Gupta, A.K. Bansal, Crit. Rev. Ther. Drug Carr. Syst. 21 (2004) 133–193.
[85] P. Debenedetti, Concepts and Principles, Princeton University Press, USA, 1996.
[86] A. Onuki, Phase Transition Dynamics, Cambridge University Press, UK, 2002.
[87] K. Binder, Rep. Prog. Phys. 50 (1987) 783.
[88] K.F. Kelton, A.L. Greer, Nucleation in Condensed matter: Applications in Materials and Biology, Elsevier, Amsterdam, Netherlands, 2010.
[89] A.S. Myerson, B.L. Trout, Science 341 (2013) 855–856.
[90] J. Russo, F. Romano, H. Tanaka, Phys. Rev. X 8 (2018) 021040.
[91] Q. Jiang, H. Shi, M. Zhao, Acta Mater. 47 (1999) 2109–2112.
[92] D. Turnbull, J. Appl. Phys. 21 (1950) 1022–1028.
[93] D.G. Fahrenheit, Philos. Trans. R. Soc. Lond. 33 (1724) 78–84.
[94] F.C. Frank, Proc. R. Soc. London Ser. A-Math. Phys. Eng. Sci. 215 (1952) 43–46.
[95] M. Rappaz, P. Jarry, G. Kurtuldu, J. Zollinger, Metall. Mater. Trans. A 51 (2020) 2651–2664.
[96] H. Reichert, O. Klein, H. Dosch, M. Denk, V. Honkimäki, T. Lippmann, G. Reiter, Nature 408 (2000) 839–841.
[97] L. Song, X. Tian, Y. Yang, J. Qin, H. Li, X. Lin, Front. Chem. 8 (2020) 607.
[98] Q. Zhang, J. Wang, S. Tang, Y. Wang, J. Li, W. Zhou, Z. Wang, Phys. Chem. Chem. Phys. 21 (2019) 4122–4135.
[99] G. Díaz Leines, R. Drautz, J. Rogal, J. Chem. Phys. 146 (2017) 154702.
[100] G.D. Leines, J. Rogal, Phys. Rev. Lett. 128 (2022) 166001.
[101] Y.C. Hu, H. Tanaka, Sci. Adv. 6 (2020) eabd2928.
[102] Y. Hu, H. Tanaka, Nat. Commun. 13 (2022) 4519.
[103] D.W. Lynch, J. Synchrot. Radiat. 4 (1997) 334–343.
[104] V. Cerantola, A.D. Rosa, Z. Konôpková, R. Torchio, E. Brambrink, A. Rack, U. Zastrau, S. Pascarelli, J. Phys.-Condes. Matter 33 (2021) 274003.
[105] A.L. Robinson, Synchrot. Radiat. News 28 (2015) 4–9.
[106] https://lightsources.org/lightsources-of-the-world/.
[107] P. Raimondi, Synchrot. Radiat. News 29 (2016) 8–15.
[108] D. Chenevier, A. Joly, Synchrot. Radiat. News 31 (2018) 32–35.
[109] P. Raimondi, C. Benabderrahmane, P. Berkvens, J.C. Biasci, P. Borowiec, J.F. Bouteille, T. Brochard, N.B. Brookes, N. Carmignani, L.R. Carver, J.M. Chaize, J. Chavanne, S. Checchia, Y. Chushkin, F. Cianciosi, M. Di Michiel, R. Dimper, A. D'Elia, D. Einfeld, F. Ewald, L. Farvacque, L. Goirand, L. Hardy, J. Jacob, L. Jolly, M. Krisch, G. Le Bec, I. Leconte, S.M. Liuzzo, C. Maccarrone, T. Marchial, D. Martin, M. Mezouar, C. Nevo, T. Perron, E. Plouviez, H. Reichert, P. Renaud, J.L. Revol, B. Roche, K.B. Scheidt, V. Serriere, F. Sette, J. Susini, L. Torino, R. Versteegen, S. White, F. Zontone, Commun. Phys. 6 (2023) 82.
[110] R.E. Dinnebier, S.J. Billinge, Powder diffraction: theory and practice, Royal Society of Chemistry, London, USA (2008).
[111] F. Frank, M. Tkadletz, C. Saringer, A. Stark, N. Schell, M. Deluca, C. Czettl, N. Schalk, Coatings 11 (2021) 264.
[112] M.D. Raven, R.W. Fitzpatrick, P.G. Self, Geol. Soc. 492 (2021) 165–179.
[113] M. Filez, E.A. Redekop, J. Dendooven, R.K. Ramachandran, E. Solano, U. Olsbye, B.M. Weckhuysen, V.V. Galvita, H. Poelman, C. Detavernier, Angew. Chem.-Int. Edit. 58 (2019) 13220–13230.
[114] A.S. Masadeh, J. Exp. Nanosci. 11 (2016) 951–974.
[115] K.S. Suslick, Encyclopedia of Physical Science and technology, Sonoluminescence and Sonochemistry, 3rd ed., 2001, pp. 1–20.
[116] C.J. Benmore, ISRN Mater. Sci. (2012) 1–19 2012.
[117] D. Lahiri, S.M. Sharma, A.K. Verma, B. Vishwanadh, G. Dey, G. Schumacher, T. Scherb, H. Riesemeier, U. Reinholz, M. Radtke, J. Synchrot. Radiat. 21 (2014) 1296–1304.
[118] J. Yano, V.K. Yachandra, Photosynth. Res. 102 (2009) 241–254.
[119] T. Sato, R. Letrun, H.J. Kirkwood, J. Liu, P. Vagovič, G. Mills, Y. Kim, C.M.S. Takem, M. Planas, M. Emons, T. Jezynski, G. Palmer, M. Lederer, S. Schulz, J. Mueller, H. Schlarb, A. Silenzi, G. Giovanetti, A. Parenti, M. Bergemann, T. Michelat, J. Szuba, J. Grünert, H.N. Chapman, A.P. Mancuso, Optica 7 (2020) 716–720.
[120] H.N. Chapman, P. Fromme, A. Barty, T.A. White, R.A. Kirian, A. Aquila, et al., Nature 470 (2011) 73–77.
[121] K. Xiang, S. Huang, H. Song, V. Bazhenov, V. Bellucci, S. Birnsteinova, R. de Wijn, J.C. Koliyadu, F.H. Koua, A. Round, E. Round, A. Sarma, T. Sato, M. Sikorski, Y. Zhang, E.M. Asimakopoulou, P. PVillanueva-Perez, K. Porfyrakis, I. Tzanakis, D.G. Eskin, N. Grobert, A. Mancuso, R. Bean, P. Vagovic, J. Mi, arXiv preprint arXiv:2305.08538 (2023). doi:10.48550/arXiv.2305.08538.
[122] S. Serkez, G. Geloni, S. Tomin, G. Feng, E. Gryzlova, A. Grum-Grzhimailo, M. Meyer, J. Opt. 20 (2018) 024005.
[123] W. Barletta, J. Bisognano, J. Corlett, P. Emma, Z. Huang, K.J. Kim, R. Lindberg, J. Murphy, G. Neil, D. Nguyen, Nucl. Instrum. Methods Phys. Res. Sect. A-Accel. Spectrom. Dect. Assoc. Equip. 618 (2010) 69–96.
[124] P. Buseck, J. Cowley, L. Eyring, High-resolution Transmission Electron microscopy: and Associated Techniques, Oxford University Press, UK, 1989.
[125] A. Hirata, L. Kang, T. Fujita, B. Klumov, K. Matsue, M. Kotani, A. Yavari, M. Chen, Science 341 (2013) 376–379.
[126] J. Miao, P. Ercius, S.J. Billinge, Science 353 (2016) aaf2157.
[127] A. Pryor Jr, Y. Yang, A. Rana, M. Gallagher-Jones, J. Zhou, Y.H. Lo, G. Melinte, W. Chiu, J.A. Rodriguez, J. Miao, Sci. Rep. 7 (2017) 10409.
[128] Y. Yuan, D.S. Kim, J. Zhou, D.J. Chang, F. Zhu, Y. Nagaoka, Y. Yang, M. Pham, S.J. Osher, O. Chen, Nat. Mater. 21 (2022) 95–102.
[129] D. Kofalt, S. Nanao, T. Egami, K. Wong, S. Poon, Phys. Rev. Lett. 57 (1986) 114.
[130] D. Kofalt, I. Morrison, T. Egami, S. Preische, S. Poon, P. Steinhardt, Phys. Rev. B 35 (1987) 4489.
[131] S. Nanao, W. Dmowski, T. Egami, J. Richardson Jr, J. Jorgensen, Phys. Rev. B 35 (1987) 435.
[132] S.J. Billinge, in: Pair Distribution Function technique: Principles and methods, Uniting Electron Crystallography and Powder Diffraction, Springer, 2012, pp. 183–193.
[133] A.K. Soper, E.R. Barney, J. Appl. Crystallogr. 44 (2011) 714–726.
[134] T. Egami, S.J. Billinge, Underneath the Bragg peaks: Structural Analysis of Complex Materials, Elsevier, Amsterdam, Netherlands, 2003.
[135] Y. Liao, Practical Electron Microscopy and Database, An Online Book, 2006 https://www.globalsino.com/EM/page3097.html.
[136] A. Sokolov, A. Kisliuk, M. Soltwisch, D. Quitmann, Phys. Rev. Lett. 69 (1992) 1540.
[137] S. Pan, J. Qin, W. Wang, T. Gu, Phys. Rev. B 84 (2011) 092201.
[138] H. Lou, X. Wang, Q. Cao, D. Zhang, J. Zhang, T. Hu, H.K. Mao, J.Z. Jiang, Proc. Natl. Acad. Sci. U. S. A. 110 (2013) 10068–10072.
[139] M.J. Cliffe, M.T. Dove, D. Drabold, A.L. Goodwin, Phys. Rev. Lett. 104 (2010) 125501.
[140] Q. Zhang, J. Li, S. Tang, Z. Wang, J. Wang, J. Phys. Chem. C 125 (2021) 3480–3494.
[141] R. McGreevy, L. Pusztai, Mol. Simul. 1 (1988) 359–367.
[142] A. Soper, Chem. Phys. 202 (1996) 295–306.
[143] R.L. McGreevy, J. Phys.-Condes. Matter 13 (2001) R877.
[144] D.T. Bowron, S.Diaz Moreno, Coord. Chem. Rev. 277–278 (2014) 2–14.
[145] A. Soper, Phys. Rev. B 72 (2005) 104204.
[146] W.Y. Wang, J.J. Han, H.Z. Fang, J. Wang, Y.F. Liang, S.L. Shang, Y. Wang, X.J. Liu, L.J. Kecskes, S.N. Mathaudhu, X. Hui, Z.K. Liu, Acta Mater 97 (2015) 75–85.
[147] R. Freitas, E.J. Reed, Nat. Commun. 11 (2020) 3260.
[148] K. Hoshino, J. Phys.-Condes. Matter 21 (2009) 474212.
[149] G. Wang, Y. Xiao, C. Zhao, J. Li, D. Shang, Metall. Mater. Trans. B 49 (2018) 282–290.
[150] P. Ganesh, M. Widom, Phys. Rev. B 77 (2008) 014205.
[151] H. Sheng, W. Luo, F. Alamgir, J. Bai, E. Ma, Nature 439 (2006) 419–425.
[152] Y. Cheng, E. Ma, H. Sheng, Phys. Rev. Lett. 102 (2009) 245501.
[153] M. Blodgett, K. Kelton, J. Non-Cryst. Solids 412 (2015) 66–71.
[154] W. Xu, M.T. Sandor, Y. Yu, H.B. Ke, H.P. Zhang, M.Z. Li, W.H. Wang, L. Liu, Y. Wu, Nat. Commun. 6 (2015) 7696.

[155] H. Tanaka, H. Tong, R. Shi, J. Russo, Nat. Rev. Phys. 1 (2019) 333–348.
[156] C. Shi, O.L. Alderman, D. Berman, J. Du, J. Neuefeind, A. Tamalonis, J.R. Weber, J. You, C.J. Benmore, Front. Mater. 6 (2019) 38.
[157] L.B. Skinner, A.C. Barnes, P.S. Salmon, L. Hennet, H.E. Fischer, C.J. Benmore, S. Kohara, J.R. Weber, A. Bytchkov, M.C. Wilding, Phys. Rev. B 87 (2013) 024201.
[158] T. Proffen, R. Neder, J. Appl. Crystallogr. 32 (1999) 838–839.
[159] P. Juhás, L. Granlund, P. Duxbury, W. Punch, S. Billinge, Acta Crystallogr. Sect. A 64 (2008) 631–640.
[160] P. Juhás, D. Cherba, P. Duxbury, W. Punch, S. Billinge, Nature 440 (2006) 655–658.
[161] F.M. Michel, L. Ehm, S.M. Antao, P.L. Lee, P.J. Chupas, G. Liu, D.R. Strongin, M.A. Schoonen, B.L. Phillips, J.B. Parise, Science 316 (2007) 1726–1729.
[162] A. Di Cicco, A. Trapananti, S. Faggioni, A. Filipponi, Phys. Rev. Lett. 91 (2003) 135505.
[163] L. Xiong, X. Wang, Q. Yu, H. Zhang, F. Zhang, Y. Sun, Q. Cao, H. Xie, T. Xiao, D. Zhang, Acta Mater. 128 (2017) 304–312.
[164] N.A. Mauro, V. Wessels, J.C. Bendert, S. Klein, A.K. Gangopadhyay, M.J. Kramer, S.G. Hao, G.E. Rustan, A. Kreyssig, A.I. Goldman, K.F. Kelton, Phys. Rev. B 83 (2011) 184109.
[165] M. Li, Y. Zhang, C. Wu, H. Geng, Appl. Phys. A 122 (2016) 1–5.
[166] X. Li, F. Zu, J. Yu, B. Zhou, Phase Transit. 81 (2008) 43–50.
[167] S. Huang, S. Luo, L. Qin, D. Shu, B. Sun, A.J.G. Lunt, A.M. Korsunsky, J. Mi, Scr. Mater. 211 (2022) 114484.
[168] Y. Zhao, S. Cao, L. Zeng, M. Xia, N. Jakse, J. Li, Metall. Mater. Trans. A 54 (2022) 646–657.
[169] S. Cao, W. Lu, Q. Hu, P. Yu, X. Ge, P. Lai, J. Li, Scr. Mater. 209 (2022) 114365.
[170] S. Cao, L. Zeng, M. Xia, P. Yu, W. Lu, J. Li, J. Mol. Liq. 357 (2022) 119143.
[171] S. Cao, L. Zeng, M. Xia, N. Jakse, P. Yu, W. Lu, J. Li, Metall. Mater. Trans. A 53 (2022) 3274–3284.
[172] P. Srirangam, M.J. Kramer, S. Shankar, Acta Mater. 59 (2011) 503–513.
[173] S. Huang, Synchrotron X-ray Operando Studies of Atomic Structure Evolution of Multi-Component Al alloys in Liquid State, University of Hull, 2023 Ph.D. Thesis.